Boiling in nanopores through localized Joule heating: Transition between nucleate and film boiling

Soumyadeep Paul, Wei-Lun Hsu, Yusuke Ito, and Hirofumi Daiguji*
Department of Mechanical Engineering, The University of Tokyo, 7-3-1, Hongo, Bunkyo-ku, Tokyo 113-8656, Japan

(Received 21 July 2022; accepted 27 October 2022; published 15 November 2022)

The transition from nucleate to film boiling on micro/nanotextured surfaces is of crucial importance in a number of practical applications, where it needs to be avoided to enable safe and efficient heat transfer. Previous studies have focused on the transition process at the macroscale, where heat transfer and bubble generation are activated on an array of micro/nanostructures. In the present study, we narrow down our investigation scale to a single nanopore, where, through localized Joule heating within the pore volume, single-bubble nucleation and transition are examined at nanosecond resolution using resistive pulse sensing and acoustic sensing. Akin to macroscale boiling, where heterogeneous bubbles can nucleate and coalesce into a film, in the case of nanopores also, patches of heterogeneous bubbles nucleating on the cylindrical pore surface can form a torus-shaped vapor film blanketing the entire pore surface. In contrast to conventional pool boiling, nanopore boiling involves a reverse transition mechanism, where, with increased heat generation, film boiling reverts to nucleate boiling. With increasing bias voltage across the nanopore, the Joule heat production increases within the pore, leading to destabilization and collapse of the torus-shaped vapor film.

DOI: 10.1103/PhysRevResearch.4.043110

I. INTRODUCTION

Despite a century of research on vapor bubble dynamics and its ramifications for boiling phenomena, a unified understanding of bubble nucleation at the nanoscale and growth/transition to macrobubbles has yet to be established. Little attention has been paid to establishing fundamental connections between boiling characteristics at the nanoscale and macroscale, which may differ significantly owing to confinement effects [1,2]. Closing this fundamental gap in knowledge is of paramount importance for fully leveraging the benefits of phase change heat transfer in high-heat-flux applications, including, among others, electronic cooling [3], inkjet printing [4], and spray quenching [5]. Starting with the work of Nukiyama [6], who heated a liquid by running electricity through a metal wire, early research in this field was devoted to establishing a boiling curve consisting of five regions of pool boiling [7]: natural convection, isolated nucleate boiling followed by slug nucleate boiling, transition boiling terminating at the Leidenfrost point, and ultimately film boiling. Research has been focused on fundamental understanding of pool boiling transitions with the aim of achieving practical goals in engineering [3,8–10], such as enhancement of the heat transfer coefficient [11] and prevention of early critical heat flux [3]. The latter is the limiting heat flux beyond which the heat transfer to the liquid starts to decrease owing to lack of liquid contact with the heated surface because of horizontal coalescence of nucleating bubbles. Other notable fundamental studies include those of micro/macroscale boiling on nano/microstructured surfaces, where high temporal and spatial resolution x-ray imaging of the vapor interface [12–15] has provided valuable insights into microscale boiling transitions.

Recently, a study by Popov *et al.* [16] using small-angle neutron scattering detected stable vapor nanobubbles of dimensions below the roughness scale on a hydrophilic boiling surface. This highlights the need for studying *subroughness* boiling, where the stability of vapor nanobubbles may hold the key to enhancing boiling heat transfer. This is especially challenging for two reasons: (i) heating must be focused such that single-bubble nucleation can be achieved; (ii) the nanoscale–nanosecond dynamics of the nanobubble post nucleation must be captured experimentally. Because of these inherent difficulties, at the nanoscale, engineering research on boiling involving heat transfer enhancement [17,18] and physics research on single-vapor bubble dynamics involving equilibrium and stability characteristics [19] have mostly proceeded in parallel but separately. On the other hand, at the macroscale, engineering studies of boiling and of single-vapor-bubble dynamics have been performed simultaneously. In this regard, we would highlight the work of Dhir and coworkers [20] in which microgravity was used to confine a macrobubble on a heater surface, thereby allowing a prolonged investigation of spherical thermal bubble dynamics. Nam *et al.* [21] studied the nucleation and departure dynamics of nucleate bubbles from a single air-filled 15 μm cavity on a superhydrophilic surface. Lee *et al.* [22] limited boiling incipience to a single microscale cavity embedded within a microchannel flow boiling apparatus. In both cases, bubble nucleations were triggered at less than 10 K wall

*Corresponding author: daiguji@thml.t.u-tokyo.ac.jp

superheats, compared with the 100 K superheat needed for 100 nm cavities [23]. This is because the geometric confinement effect becomes critical at sub-micrometer scales, where boiling becomes more explosive owing to high surface tension dominance. For example, Levine *et al.* [24] found an inertial homogeneous bubble growth velocity of 50 m/s in a 107-nm diameter pore, compared with the 0.5 m/s seen in a 16.4 μm cavity by Lee *et al.* [22]. Also, Nam *et al.* [21] reported that the contact line of the nucleating bubble extended beyond the cavity diameter, with bubble departure occurring at 1-mm length scales. This also suggests that geometric confinement is less significant at the microscale. It should be noted here that both Nam *et al.* [21] and Lee *et al.* [22] observed bubbles at 100 μm length scales, which overshadowed the boiling characteristics within the cavity. This is of course extremely difficult to realize using traditional imaging and requires nonconventional approaches.

Despite the obvious challenges, several studies have partly addressed this question. For example, Wang *et al.* [25] generated plasmonic vapor bubbles on a nanoparticle array through laser heating and imaged bubble growth post nucleation at 7.47 MHz using a high-speed camera. However, the minimum bubble size imaged by their system was in the 5 μm range, which was outside the scope of nanoscale bubble growth dynamics. In a similar vein, Hou *et al.* [26] also used a laser to initiate plasmonic vapor bubble nucleation on a single nanoparticle. By measuring the laser scattering using a photodetector, they were able to obtain signals corresponding to nanobubble growth speeds. However, probing the orientation or shape of a bubble on a particle is quite difficult, since the laser beam width is much larger than both the particle and bubble. Nag *et al.* [27] used radiolysis to generate gas nanobubbles in a liquid cell placed inside a transmission electron microscope (TEM). Although interesting phenomena related to nanobubble coalescence were observed, the growth speed of the bubbles was much slower than that of vapor bubbles. Similar slow gas bubble dynamics were also observed using scanning electrochemical cell microscopy [28], nanoelectrodes [29,30], and nanopipettes [31]. This highlights the fact that compared with gas nanobubbles, vapor nanobubbles are more difficult to measure, since their dynamics take place at nanosecond time resolutions. To solve this problem, Fu *et al.* [32] used 4D TEM to image vapor bubble nucleation and growth on a single nanoparticle at high spatial and time resolutions commensurate with nanoscale vapor bubble dynamics. However, their system has a high setup and operational cost, elevating the threshold for investigation by other groups.

To activate single-bubble nucleation, we utilize Joule heating, which directly converts electric energy to thermal energy in confined liquid volumes, circumventing interfacial heat transfer. Nagashima *et al.* [38] filled a concentrated electrolyte solution in a nanopore connected with two large solution reservoirs. An electric potential bias was imposed across a membrane of thickness 71 nm via electrodes inserted in each side of the reservoir. The electric field was focused around the nanoaperture on the thin membrane, generating intense Joule heating in the nanospace. Homogeneous thermal bubble generation in the liquid phase was successfully detected via ionic current measurements in the gigahertz bandwidth of resistive pulses, based on the volume exclusion effect of nonconductive bubbles. This method of bubble generation and detection overcomes both the scale and time limitations of traditional boiling studies using heater surfaces and high-speed cameras, thereby serving as an ideal platform for tracking single nanobubbles in the initial stage of boiling. Using the same platform, Paul *et al.* [39] demonstrated that solely homogeneous nucleation occurs only in tiny apertures at the nanoscale. As the pore diameter expands, heterogeneous bubbles originating from the inner walls of nanopores become dominant. This transition was attributed both to geometric confinement effects such as contact line pinning and to a thermal confinement effect, namely, a large temperature gradient within the nanopore.

In the present paper, we measure both ionic current variations and stress waves created by a nanopore bubble [Figs. 1(a) and 1(b)], focusing specifically on the transition between nucleate and film boiling. Here, we should highlight that although current blockage signals and pressure waves have been used separately to study single-bubble nucleation [28–31,38] and bubble dynamics at the microscale [36,37,40–43], they have not previously been used simultaneously to explain high-speed nanoscale boiling transitions postnucleation. This could be very effective in discriminating boiling structures within the pore. By intensifying the heating rate through increasing the bias voltages across the nanopore, we activate the transition from nucleate boiling to heterogeneous film boiling on the rim of the nanopore. Owing to the cylindrical shape of the pore, the film bubble resembles a torus in shape, as shown in Fig. 1(c) (Appendix A). A similar observation has also been made by Medvedev *et al.* [44], albeit at the macroscale. Nanobubbles on flat surfaces have already been shown to exhibit remarkable stability owing to the contact line pinning effect [45,46], and here we demonstrate that nanotorus thermal bubbles also exhibit stability owing to similar pining effects within nanopores. Unlike nucleate bubbles, which undergo rapid growth and collapse cycles separated by significant reheating periods, the film bubble is stable and relatively long lived, undergoing pinned volumetric oscillations, which are captured by our sensors in the form of pore current and hydrophone pressure oscillations. When the bubble is moderately stable, the oscillations are weakly nonlinear [47,48], and only the fundamental and second harmonics are observed beyond the noise level of our sensors. The 3D spectrogram analysis of the torus bubble presented in Fig. 1(d) reveals two ridges at 6 MHz and 12 MHz, which correspond to these two harmonics. These frequencies are an order of magnitude higher than those recorded for oscillatory boiling on microheaters [36], probably owing to the larger bubble size compared with a nanopore bubble. Intriguingly, our voltammetric studies reveal that for larger pore diameters, with increasing voltage, the torus bubble gradually loses its stability, ultimately leading to transition from film to nucleate boiling.

In this paper, we showcase the similarities in bubble dynamics and thermodynamics between macroscale pool boiling and nanopore boiling, while also highlighting the differences in the thermofluidic mechanisms driving the transitions. The remainder of the paper is organized as follows. In Sec. II, a brief overview of our experimental system is presented. Section III B explains the nucleate-to-film boiling transition using current and hydrophone pressure spectrograms for a

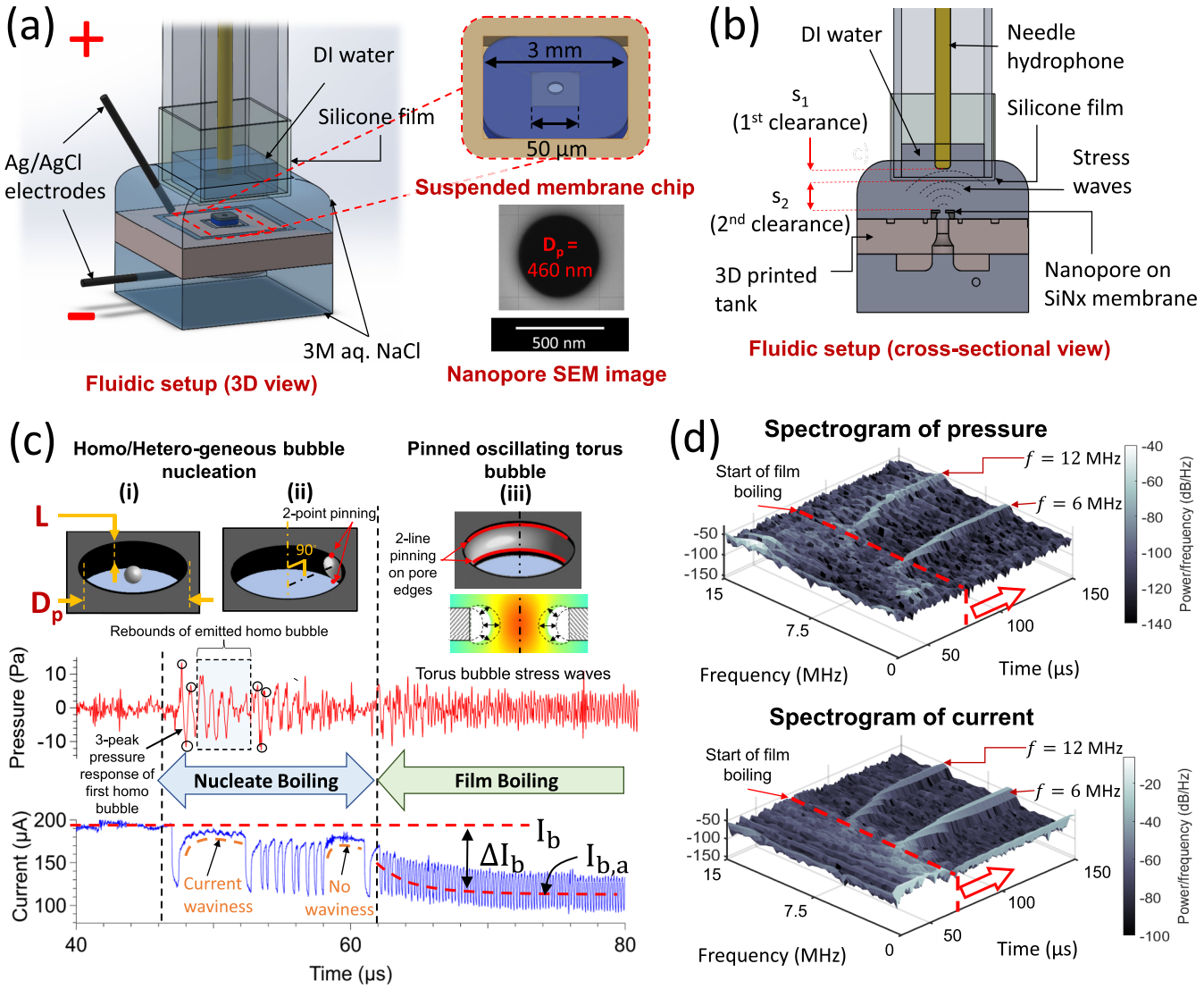

FIG. 1. (a) 3D schematic view and (b) cross-sectional schematic view of the acoustic and resistive pulse sensing experimental setup. The insets in (a) show a schematic of the suspended membrane nanopore chip (a cylindrical hole of diameter D_p on a silicon nitride thin layer of thickness L) and an SEM image of the $D_p = 460$ nm nanopore. (c) Nanopore current (blue) and hydrophone pressure (red) traces during nanopore boiling during a 1468 µs–7 V voltage pulse starting from $t = 0$ µs. Before 46 µs, when there is only superheating and no boiling, both the current and pressure baselines are steady. This is followed by stochastic nucleate boiling, when two processes of bubble generation are predominant: (i) homogeneous bubble nucleation at the pore center and (ii) patch heterogeneous bubble nucleation on the pore surface. Here, discrete homogeneous and heterogeneous bubbles grow and shrink, nonperiodic current blockage signals are seen in the current trace, and high-amplitude nonperiodic pressure waves are observed. For each of these discrete bubble events, a three-peak acoustic wave is created, wherein the three peaks denote the inertial growth, condensation driven retardation and bubble collapse regimes respectively [33–35]. Also, the baseline current is recovered after each blockage event, which indicates that the pore is bubble free, allowing Joule heating until the next nucleation event after a waiting time. When nucleate boiling transitions to film boiling after ~16 µs, a torus-shaped vapor bubble blankets the nanopore wall surface (iii). This bubble then performs pinned volumetric oscillations in thermal resonance [36,37] with the Joule heat generation inside the pore liquid. Owing to the stability of the torus bubble of volume comparable to the pore volume V_p, the baseline current steadily decreases by ~42% from I_b to $I_{b,a}$. The large shift in current baseline (ΔI_b) for a pore with a high D_p/L ratio (= 4.6) can be explained by the existence of a torus bubble that has a volume V_b scaling proportionally with the pore diameter. Owing to the high sensitivity of the nanopore current to the insulating bubble, oscillations of the bubble volume about its mean value are represented by near-sinusoidal current oscillations about the reduced baseline $I_{b,a}$. Consequently, the hydrophone also picks up high-frequency and periodic pressure waves generated as a result of bubble volume oscillations. (d) 3D spectrogram analysis of the nanopore current and hydrophone pressure. During nucleate boiling with stochastic waiting times, the power spectrum is distributed across a wide frequency band, and hence no clear frequency ridges are seen in the spectrograms. After the film boiling transition at ~62 µs, when the torus bubble oscillates at a characteristic frequency, two ridges are seen at $f = 6$ MHz and 12 MHz, signifying the first and second harmonics, respectively.

420-nm pore, and Sec. III C elucidates the film-to nucleate boiling transition in a 460-nm pore. Section IV A discusses the effect on Joule heat generation during the different nanopore boiling regimes for the two pore sizes. In macroscale film boiling, the vapor film limits heat *transfer* from the heated surface, whereas in nanopore boiling, the torus vapor film limits Joule heat *production* through the volume exclusion effect. In Sec. IV B, a theoretical model is developed to capture the equilibrium size and temperature of the torus vapor film at different applied voltages. In Sec. IV C, the stability of the torus vapor film is analyzed by perturbation theory, and the reverse transition phenomenon (film-to-nucleate boiling) is explained based on this analysis. Conclusions are presented in Sec. V.

II. EXPERIMENTAL METHODS

Circular nanopores as shown in the scanning electron microscope (SEM) image in Fig. 1(a) and in Fig. S1 of the Supplemental Material [49] were made on silicon nitride chips (Model No. 4088SN-BA) purchased from Alliance Biosystems Inc., each comprising a 100-nm-thick silicon nitride (Si_3N_4) membrane deposited on a 200-μm-thick silicon substrate with an approximately square 50 μm × 50 μm opening at the center. The nanopores were etched at the center of the free-standing part of the membrane using a focused Ga^+ ion beam (SMI2050MS2, SII Nanotechnology). Post fabrication, the nanopore chip was assembled between two fluid tanks and wetted with ethanol before flushing with a 3M aqueous solution of NaCl prepared by diluting 5M NaCl solution (Sigma-Aldrich) with deionized (DI) water. Voltage pulses were applied through Ag/AgCl electrodes using a pulse generator (Tektronix AFG3152C), and the ionic current flowing through the nanopore was registered on a oscilloscope (Tektronix MSO56) by measuring the voltage across a shunt resistor through an active power rail probe at 20 MHz terminal bandwidth (Tektronix TPR4000). In addition, a passive probe set at 250 MHz terminal bandwidth was used to measure high-frequency current oscillations across a second shunt resistor in series. The active probe, which had a high signal-to-noise ratio but also high capacitance, was used to track the baseline and frequency shifts of the nanopore current, while the passive probe measurements taken at high bandwidth were used to measure the amplitude of current oscillations. A needle hydrophone (Precision Acoustics NH4000 with sensor diameter 4 mm, or Precision Acoustics NH1000 with sensor diameter 1 mm) encapsulated in a hollow quartz cell was also placed vertically above the chip surface to collect the stress waves from the nanopore bubbles at 20 MHz terminal bandwidth. Unless otherwise mentioned, the acoustic results shown in this paper were captured using the NH4000 hydrophone, which has a higher sensitivity. The stress waves collected by the piezoelectric sensor were converted into electrical signals by a preamplifier and DC coupler, which were registered in the oscilloscope concurrently with the current signals. To shield the piezoelectric element of the hydrophone from the ionic current, the hydrophone was encapsulated in a custom-made glass shell filled with DI water. A 20-μm-thick silicone film (Wacker Asahikasei Silicone) [Fig. 1(b)] separated the DI water from the salt solution, allowing acoustic signals to pass. Hydrophobic tape (3M Microfluidic Diagnostic Tape 9965) was used to seal the junction of the silicone film and quartz cell to prevent any electrolyte leakage. As a result of hydrophone encapsulation, the clearance distance between the piezoelectric sensor and the nanopore ($s = s_1 + s_2$) had two components, s_1 and s_2 [Fig. 1(b)]. The distance between sensor and silicone film s_1 was measured by an optical microscope, while s_2 was measured first using a contact-type distance sensor and this measurement was validated based on the delay time between the current dip and the hydrophone peak signal for homogeneous bubble nucleation (see Sec. S2 in the Supplemental Material [49]). To measure the low-intensity stress waves emanating from torus bubble oscillations at an acceptable signal-to-noise ratio, the net clearance needed to be as small as possible. For the 460-nm pore experiments detailed in Figs. 1 and 6, $s = 500 \pm 20$ μm. Owing to the large difference between sensor diameter and clearance distance, the spatial averaging effect [50] distorted the actual stress wave amplitude. Nonetheless, a qualitative analysis of pressure amplitudes for varying voltages and varying bubble frequencies still provides insight into the bubble dynamics.

The acoustic signals registered in the oscilloscope as voltage signals $V_p(t)$ were then converted into pressure waveforms using the following equation [51]:

$$p(t) = F^{-1}\left\{\frac{F\{V_p(t)\}}{M(f)}\right\}, \tag{1}$$

where F and the F^{-1} operators denote the Fourier and inverse Fourier transforms, respectively, and $M(f)$ is the frequency response of the hydrophone sensitivity as per plane wave calibration measurements performed by the manufacturer, Precision Acoustics. The uncertainty in $M(f)$ was in the range 19–22%. The imaginary part of the acoustic pressure $p(t)$ obtained after inverse Fourier transform is neglected.

III. RESULTS

Single-bubble boiling is activated by localized Joule heating inside a submicrometer pore on a 100-nm-thick suspended silicon nitride membrane [Fig. 1(a)]. The nanopore is submerged inside a 3M NaCl electrolyte solution, which leads to ionic current flow once bias voltages are applied across it through Ag/AgCl electrodes. When homo- or heterogeneous bubbles are nucleated beyond their respective superheating limits, the ionic current is altered, and these changes are measured by a high-bandwidth oscilloscope. In addition, an encapsulated piezoelectric hydrophone on top of the nanopore chip [Fig. 1(b)] absorbs the stress waves generated by bubble motion and converts them into an electrical signal to be recorded in the oscilloscope simultaneously. By studying the amplitude and frequency variations of current and hydrophone pressure, we can track the boiling transition within the pore. The current signals are most sensitive to bubble dynamics within the pore, where minor changes in bubble volume modulate the pore cross-section significantly. Meanwhile, the hydrophone sensor catches any stress waves in the liquid generated by bubble expansion or shrinkage, irrespective of the bubble position relative to the pore.

A. Bubble discrimination methodologies

Previous studies on microscale boiling [33,33,36,37,52] have imaged microbubble dynamics at a length scale of 10 μm using sophisticated high-speed imaging equipment [53] at 10 million frames per second. Even then, the resulting image is blurry, and limited information can be gleaned from such imaging. This difficulty is compounded when we further reduce the length scale below the 1 μm limit. Hence, we follow a novel methodology to circumvent the spatial and temporal resolution problems of optical imaging. Both current blockage signals and acoustic signals can be acquired at nanosecond resolutions in oscilloscopes. However, differentiating between homogeneous bubble dynamics, patch heterogeneous bubble dynamics, and torus film bubble oscillations on current signals alone is complicated and has not yet been established completely. On the other hand, notable studies have benchmarked acoustic signals for single-nucleate-microbubble dynamics [33] and single-microbubble oscillation spectra [36,37,54] against direct imaging. Accordingly, we compare the acoustic signal of nanobubbles with the existing literature, on the basis of which we benchmark the current signals for nucleate and film boiling at the nanoscale. Here, it should be noted that current signals have a higher signal-to-noise ratio than acoustic signals, making them more useful for distinguishing boiling structures inside smaller nanopores.

1. Nucleate bubble dynamics

The growth and collapse cycle of a nucleate bubble has been widely studied from the macroscale to the microscale. Here, we should cite the paper of Lajoinie *et al.* [33], who studied vaporization of a laser-irradiated 3 μm capsule. A three-peak pressure wave was observed and benchmarked against high-speed imaging of a *single* heterogeneous nucleate microbubble undergoing a growth and collapse cycle. Zhao *et al.* [40] and Glod *et al.* [42] studied boiling on a 100 μm flat heater and a 10 μm diameter Pt wire respectively and correlated the three-peak acoustic wave with the explosive growth and collapse cycle of a spherical vapor bubble after a heating period. Versluis *et al.* [34] found that the growth and collapse of a macroscale homogeneous cavitation bubble also created a three-peak acoustic wave. On the basis of these previous studies, it is safe to assume that a three-peak pressure wave represents the spherical growth and collapse cycle of a single bubble postnucleation.

We study nucleate boiling inside a 1134-nm diameter pore under a 7-V voltage pulse using a hydrophone with 1 mm sensor diameter placed at a large clearance of $s = 7.9$ mm to accurately capture the sharp acoustic peaks [34] associated with explosive bubble growth and collapse [35]. A large clearance and smaller hydrophone tip diameter were chosen to avoid the spatial averaging effect [50], allowing the distortion-free acoustic wave measurement needed for identifying single-microbubble acoustic characteristics. Following the onset of the voltage pulse, a current blockage event is seen after a heating time during which a bubble nucleates within the pore. In the hydrophone pressure trace, a three-peak pressure wave is seen [Figs. 2(b) and 2(d)]. The heating time and current blockage duration for the first bubble event in the time sequence (onset of nucleate boiling, ONB) for multiple

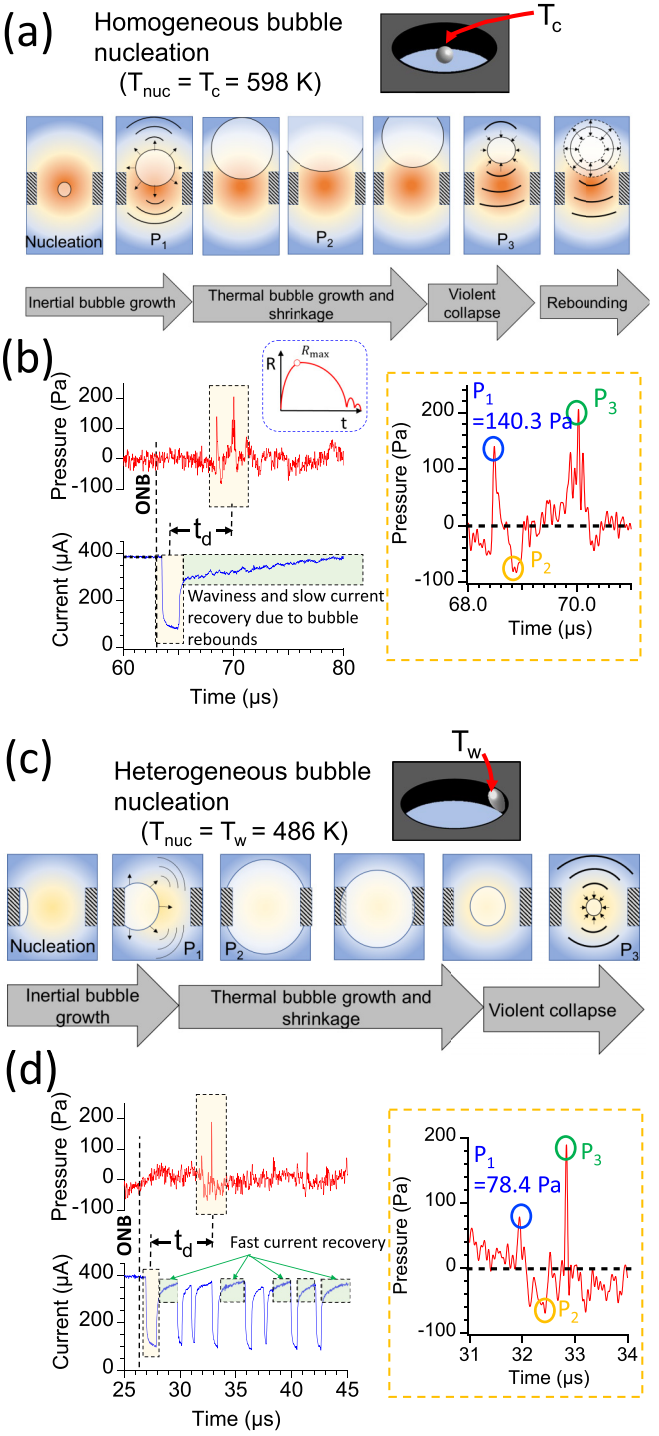

FIG. 2. Nucleate bubble dynamics. [(a),(c)] Schematic overview of homogeneous and patch heterogeneous bubble dynamics. [(b),(d)] Current and pressure signals for these bubbles as observed in a 1134-nm diameter pore under a 7-V voltage pulse.

voltage pulses are shown in Fig. S3 in the Supplemental Material [49]. Out of 80 voltage pulses, 56 resulted in the first blockage signal observed deterministically after a heating time in the interval $t_{nuc} = [61.2\ \mu s, 66.3\ \mu s]$, while for the remaining 24 voltage pulses, early stochastic nucleation was observed in the interval $t_{nuc} = [3.0\ \mu s, 43.5\ \mu s]$ (Fig. S4a in the

Supplemental Material [49]). Using Joule heating simulations (Appendix A), we obtained the transient development of the pore center and pore surface temperatures T_c and T_w, respectively [Fig. S4(b)]. In our previous paper [39], we established that nanopore Joule heating leads to either homogeneous or patch heterogeneous nucleation, with the homogeneous nucleations taking place at a considerably higher temperature of ~600 K [24,38,39] and the heterogeneous nucleation taking place within a range of 472 ± 35 K according to Witharana *et al.* [23]. The deterministic nucleation events occurring at $t_{nuc} = [61.2, 66.3]$ μs can thus be considered as homogeneous nucleations, because they occurred when T_c reached 598 K [Fig. S4(b)]. In Fig. S4(c), we segregate the two types of bubble nucleations and plot their respective nucleation temperatures. The box plot of heterogeneous nucleations on the pore surface shows a stochastic but low nucleation temperature range ($T_{nuc} = [378\,\text{K}, 516\,\text{K}]$ in Fig. S4c), which largely agrees with the range given in Witharana *et al.* [23] for a 90-nm-diameter cavity.

After differentiating between homogeneous and heterogeneous bubble nucleation events, we study their subsequent dynamics by analyzing the acoustic waves that they create. Figures 2(b) and 2(d) show the current and acoustic response for typical homogeneous and heterogeneous nucleated bubbles. For both bubbles, a three-peak (P_1, P_2, and P_3) pressure response signifying inertial growth, condensation retardation, and bubble collapse [40] of a single spherical bubble is seen to follow the current blockage signal after a constant delay time t_d. Using a 1D-moving boundary method, we have shown in our previous paper [35] that the nanopore homogeneous bubble undergoes a growth–collapse cycle with maximum bubble radius in the 1–10 μm range. This has been also established by previous studies of explosive boiling on micro- to macroscale heater surfaces [33,40,42]. The presumed homogeneous and heterogeneous bubble dynamics are explained in the schematics shown in Figs. 2(a) and 2(c), respectively. Post-bubble nucleation, the bubble grows inertially at a speed $\dot{R}_0$ that depends on the nucleation temperature according to $\dot{R}_0 = \sqrt{\frac{2}{3}[P_v(T_{nuc}) - P_w]/\rho_w}$ [19]. As the heterogeneous bubble nucleates at a lower temperature ($T_{nuc} = 486$ K) than the homogeneous bubble ($T_{nuc} = 598$ K), the inertial growth speed will be lower for the heterogeneous bubble ($\dot{R}_0 = 36$ ms^{-1}) than the homogeneous bubble ($\dot{R}_0 = 89$ ms^{-1}). This would lead to more explosive bubble growth for the homogeneous bubble, creating a higher inertial growth pressure peak P_1. It should be noted here that the static pressure at the hydrophone tip is proportional to the square of the growth velocity $\dot{R}$ and is given by $P_s = (\rho R/s)(2\dot{R}^2 + R\ddot{R})$, where R is the bubble radius and $\ddot{R}$ is the bubble acceleration. In accordance with the theory, our experiments also show a higher $P_1 = 140.3$ Pa for the homogeneous bubble [Fig. 2(b), inset] compared with $P_1 = 78.4$ Pa for the heterogeneous bubble [Fig. 2(d), inset].

In summary, discrete bubbles having three-peak pressure waves can be defined as following *single* nucleate bubble dynamics. For these bubbles, current blockage signals have unequal waiting times, owing to the stochastic heterogeneous nucleation temperatures [23] [Fig. S4(c)], and the baseline current is recovered after each event owing to the collapse of the bubble. Owing to the unequal waiting times, the sensible heat stored prior to heterogeneous bubble nucleations varies, which leads to nonuniform bubble sizes, lifetimes, and blockage durations [Fig. S4(a)]. The stochastic nucleation temperatures and bubble sizes also lead to nonuniform pressure peaks for patch heterogeneous bubbles. This results in nonharmonic current and hydrophone pressure spectra, which can be taken as a distinguishing characteristic of nanoscale nucleate boiling [Fig. 3(a)].

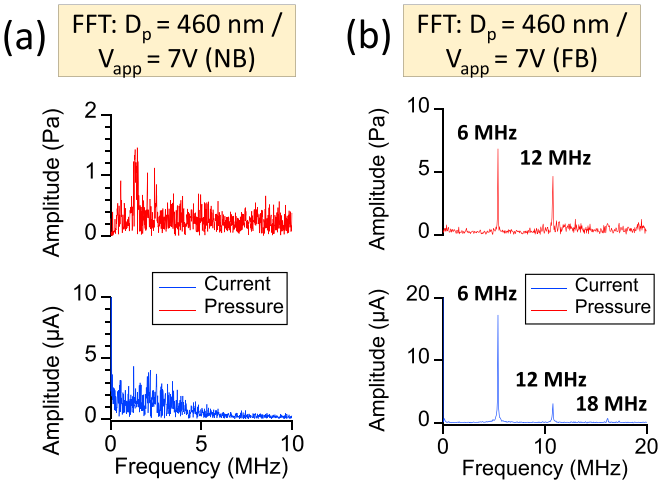

FIG. 3. Fast Fourier transform (FFT) of current and pressure signals during (a) stochastic/nonperiodic nucleate boiling (NB) and (b) harmonic film boiling (FB) for the 460-nm pore under 7-V bias voltage.

2. *Film bubble oscillations*

Nguyen *et al.* [37] studied film bubble oscillations on a electric microheater. The bubbles underwent pinned volumetric contact angle oscillations in thermal resonance with the incoming heat flux on the heater surface. These authors found sinusoidal or harmonic oscillations in the acoustic spectrograms, which were benchmarked against high-speed camera imaging of a single hemispherical bubble undergoing volumetric oscillations. Although the typical bubble had a length scale (20 μm) two orders of magnitude greater than the pore dimensions (100 nm) used by us, the same correlation between harmonic spectrograms and volumetric oscillations can be expected at the nanoscale as well. At the nanoscale, Orrit and coworkers have correlated harmonic spectrograms of photocurrent scattering with volumetric oscillations of the vapor film on single nanoparticles [55,56]. Theoretically, it was already established in Lauterborn and Kurtz's review paper [48] that single-bubble volumetric oscillations result in harmonic spectrograms.

Figures 1(c) and 1(d) show harmonic oscillations in the nanopore current and pressure starting from ~62 μs. Previous studies have suggested that these are caused by the oscillations of a single bubble. In our nanopore system this can either be (i) a spherical homogeneous bubble at the pore entrance or (ii) a patch heterogeneous bubble pinned on the pore edges or (iii) a torus-shaped vapor film pinned on the pore circumference. Possibility (i) is represented by the recovery current waviness and rebounding stress waves due to the rebounds [48,57] of

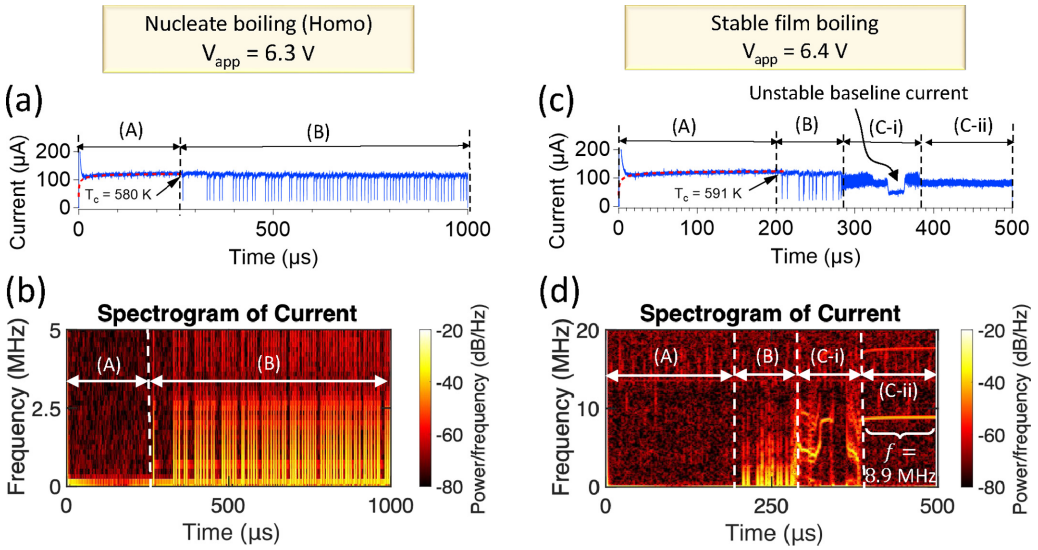

FIG. 4. Boiling transition with increasing bias voltage for a $D_p = 420$ nm pore. [(a),(b)] Nucleate homogeneous boiling at 6.3 V. [(c),(d)] Transition to stable film boiling at 6.4 V. (a) and (c) are plots of the transient shift in baseline current during the voltage pulse, while (b) and (d) are spectral bifurcation diagrams (spectrograms) of the current corresponding to the bubble oscillation frequency.

emitted homogeneous bubbles from the nanopore, as can be seen in Figs. 1(c), 2(a), and 2(b), and in Fig. S2(a) in the Supplemental Material [49]. The current amplitude is small, probably because the bubble is out of the nanopore where the pore current is less focused and is thus less affected by the bubble size. The rebounds eventually die out from viscous losses, since there is not enough Joule heating outside the pore volume. On the other hand, steady-state oscillation spectrograms are seen in our experiments [Fig. 1(d)], which indicates that the bubble is pinned inside the pore, where the Joule heating helps sustain the oscillations for thousands of cycles. This is quite different from possibility (i).

Now, a patch hemispherical bubble is not likely to be in stable equilibrium, since the bubble axis of symmetry is perpendicular to the pore axis [shown in yellow in Fig. 1(c)(ii)]. As the nanopore temperature distribution is symmetric about the pore axis, this will cause an asymmetric temperature distribution on the bubble surface. In addition, the patch bubble, owing to its higher curvature, will lose equilibrium easily under a small perturbation, through a mechanism called the Laplace pressure bubble catastrophe [58]. This causes it to undergo out-of-equilibrium growth and collapse cycles, as is evident from the three-peak response in Fig. 2(d). On the other hand, the torus bubble has an axis of symmetry that coincides with the pore axis [Fig. 1(c)(iii)], which allows the possibility of thermal resonance with Joule heating. Also, the torus bubble is pinned along the two contact lines on the pore edges, making it more stable than the the patch bubble, which is subject to only two-point pinning at the pore edges [Fig. 1(c)(ii)]. In Fig. 3(b), we find that the first- and second-harmonic frequencies (6 MHz and 12 MHz) of the nanopore current and hydrophone pressure match each other, which points toward harmonic oscillations of the bubble. Theoretically, Dockar *et al.* [59] showed that the adiabatic oscillation frequency of a hemispherical bubble on a 100 nm flat surface is in the region of 450 MHz. This, being almost two orders of magnitude higher than the experimentally observed first-harmonic frequency of 6 MHz [Fig. 3(b)], challenges the possibility of patch bubble oscillations. In addition, we have found that the permanently decreased baseline current during oscillating current signals (Fig. S19c [49]) matches the simulated steady-state current (Fig. S8b [49]) when a torus bubble is inserted on the pore walls (further explanation provided in Sec. IV B). This suggests the existence of a torus bubble inside the pore during steady-state oscillations.

B. Nucleate-to-film boiling transition

Figure 4 shows the boiling structure of a $D_p = 420$ nm pore. The current–time traces in (a) and (c) show baseline current changes, and the spectrograms (short-time averaged fast Fourier transform) in (b) and (d) show frequency changes, both providing phenomenological evidence of nucleate-to-film boiling transition.

When a voltage pulse of 6–8 V is triggered, ionic current flowing through the nanopore liberates Joule heat [60,61], which transiently increases the nanopore temperature at a rate of $\sim 10^7$ K/s from ambient conditions of 298 K [35]. As the temperature rises, the ionic conductivity increases, allowing more current flow and Joule heat generation in a feedback loop. Unlike pool boiling, where the substrate temperature can be controlled directly, in this case modulating the bias voltage only allows us to control the heat generation rate, which can reach $\sim 10^{16}$ W/m^3 [35,62]. Owing to the rate of high heating within the confined space, a temperature gradient of the order of 1 K/nm develops within the pore, which allows bubbles of different volumes and temperature to exist in thermal equilibrium within the pore liquid.

The current response to each pulse comprises an initial heating zone (A) followed by a nucleate boiling zone (B), ultimately leading to torus film boiling (C). At 6.3 V, except for an outlier (see Fig. S19 in the Supplemental Material [49]), only zones A and B are present during boiling [Figs. 4(a) and 4(b)]. However, with a 6.4-V voltage pulse, all three zones can

be identified, as shown in Figs. 4(c) and 4(d). This scheme is seen for multiple voltage pulses of the same magnitude. Thus, there is an increasing probability of film boiling transition as the voltage is increased from 6.3 V to 6.4 V.

In zone A, the Joule heat generation within the pore is balanced by heat dissipation by the silicon nitride membrane and surrounding electrolyte. No bubble-induced current blockage signals are seen, and the spectrograms also show no effect [Figs. 4(a) and 4(b)]. Zone A terminates with nucleation of a homogeneous bubble at the pore center when the local temperature reaches $T_c \sim 590 \pm 10$ K. This temperature estimate was obtained through numerical simulations, by fitting the experimental nanopore current [the red trace in Fig. 4(a)] as described in Appendix B. Before this bubble nucleation, although the pore surface temperature matches the patch heterogeneous nucleation temperature of 472 ± 35 K [23], these bubbles are suppressed. Our previous paper [39] on this topic showed that during Joule heating, unstable vapor clusters can form homogeneously at the pore center with temperature T_c and heterogeneously on the pore surface with temperature T_w. Depending on the value of the cross-pore temperature difference $\Delta T_p = T_c - T_w$, a cluster ripening competition is established between these two cluster groups at the two nucleation sites. When ΔT_p is higher, homogeneous cluster growth requires less free energy to grow, and hence the heterogeneous clusters are suppressed.

Figure 4(a) shows only the nucleate boiling regime (B) involving quasiperiodic homogeneous bubble formation and ejection at 6.3 V for a 420-nm pore. It should be noted that unlike patch bubbles, which grow and collapse in a pinned state [39,45,63] on the pore surface, the homogeneous bubbles are ejected from the pore by the electric field force acting on its negatively charged surface (the typical surface charge is $-23\,\mathrm{mCm}^2$ [31]). The homogeneous bubble is retained near the pore access region, where it rebounds spherically and volumetrically, emitting high-amplitude stress waves. Additionally, owing to the limited influence of bubble volume fluctuations on the ion current in the pore access region, low-amplitude current waviness is seen in the reheating current trace [Fig. 1(c)] after the first growth cycle post nucleation [48]. This phenomenon is illustrated in Fig. 2(b) and in Fig. S2 of the Supplemental Material [49]. On the other hand, the short-duration bubble nucleating at 58 μs [Fig. 1(c)] shows no waviness in the current recovery trace post blockage spike. This is characteristic of a patch heterogeneous bubble nucleating on the pore surface and incapable of departure owing to the strong contact line pinning force at the nanoscale. This is markedly different from pool boiling, where macroscale heterogeneous bubbles easily depart from the nucleation site owing to buoyancy.

The transition from nucleate to film boiling is seen in Fig. 4(c). Following zone B, zone C-i starts, during which the baseline current decreases but does not stabilize. In addition, the spectrograms in Fig. 4(d) show unstable frequency bands in this zone. Compared with zone B, the frequency bands are discrete but unsteady, indicating that a single unstable torus bubble is oscillating within the pore. In this regime, the torus bubble is not in thermal equilibrium with the Joule heating, which leads to rapid variations in the mean bubble size, in addition to highly nonlinear volumetric pinned oscillations

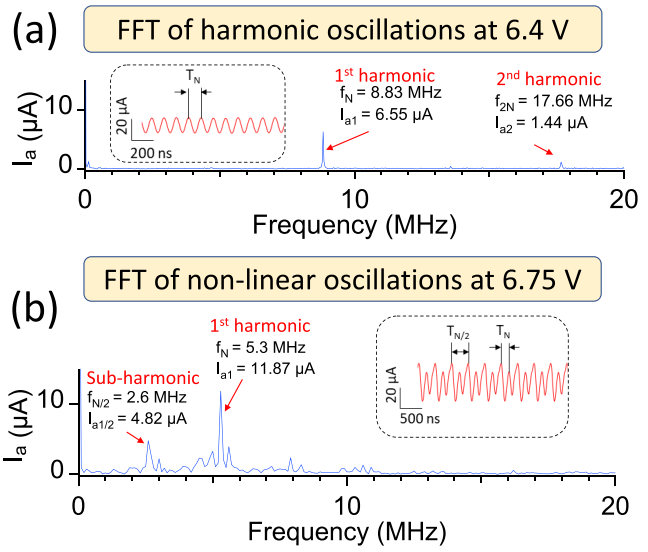

FIG. 5. Fast Fourier transform (FFT) of current signals during (a) steady-state harmonic torus bubble oscillations at 6.4 V and (b) nonlinear oscillations with subharmonic frequencies at 6.75 V for the 420-nm pore. Insets show eighth order Fourier-series fitted (at R-squared of ~87%) to the oscillating current traces. f_N and T_N denote the resonant frequency and time period, while $f_{N/2}$ and $T_{N/2}$ denote the sub-harmonic frequency and time period.

about the mean size. Eventually, the torus bubble reaches the equilibrium size corresponding to the applied voltage, and the current oscillations stabilize about a stable mean value. This marks the beginning of the stable oscillatory torus boiling regime (C-ii). In this regime, the baseline current stabilizes, and the current and pressure spectrograms show steady and narrow frequency bands. This regime continues until the end of the voltage pulse. For the 420-nm pore [Fig. 4(d)], there is a stable oscillation frequency of 8.9 MHz, whereas for the 460-nm pore [Fig. 6(b)], there is a pseudostable oscillation frequency of 4.3 MHz. Even in this regime, low-power frequency bands at secondary harmonics are also seen, indicating that the oscillations are weakly nonlinear [47]. For the 420-nm pore, we also performed a boiling structure analysis at 6.5 V and 6.75 V. We found that the stable oscillation zone (C-ii) essentially disappeared and was replaced by low-frequency (~5 MHz) nonlinear oscillations indicative of an unstable torus bubble (C-i) (Fig. S21 [49]). In Fig. 5, we can see that the 6.4 V torus bubble shows weakly nonlinear oscillations with small-amplitude first harmonic at 8.83 MHz, $I_{a1} = 6.55\,\mu\mathrm{A}$, which is 4.5 times the second harmonic at $I_{a2} = 1.44\,\mu\mathrm{A}$. In comparison, the 6.75 V torus bubble shows oscillations with large amplitude at the first harmonic of 5.3 MHz, $I_{a1} = 11.87\,\mu\mathrm{A}$, along with a subharmonic detected at 2.6 MHz and $4.82\,\mu\mathrm{A}$. The emergence of subharmonics and the shifting of the first-harmonic (main resonance) peak to a lower frequency are indications of nonlinear oscillations [47,48,64–66]. This gradual loss of torus stability with voltage is more prominent for the 460-nm pore and is discussed in Sec. III C. A similar observation was also made by Li *et al.* [36] for laser-powered heaters, where, with increasing laser power, the oscillations

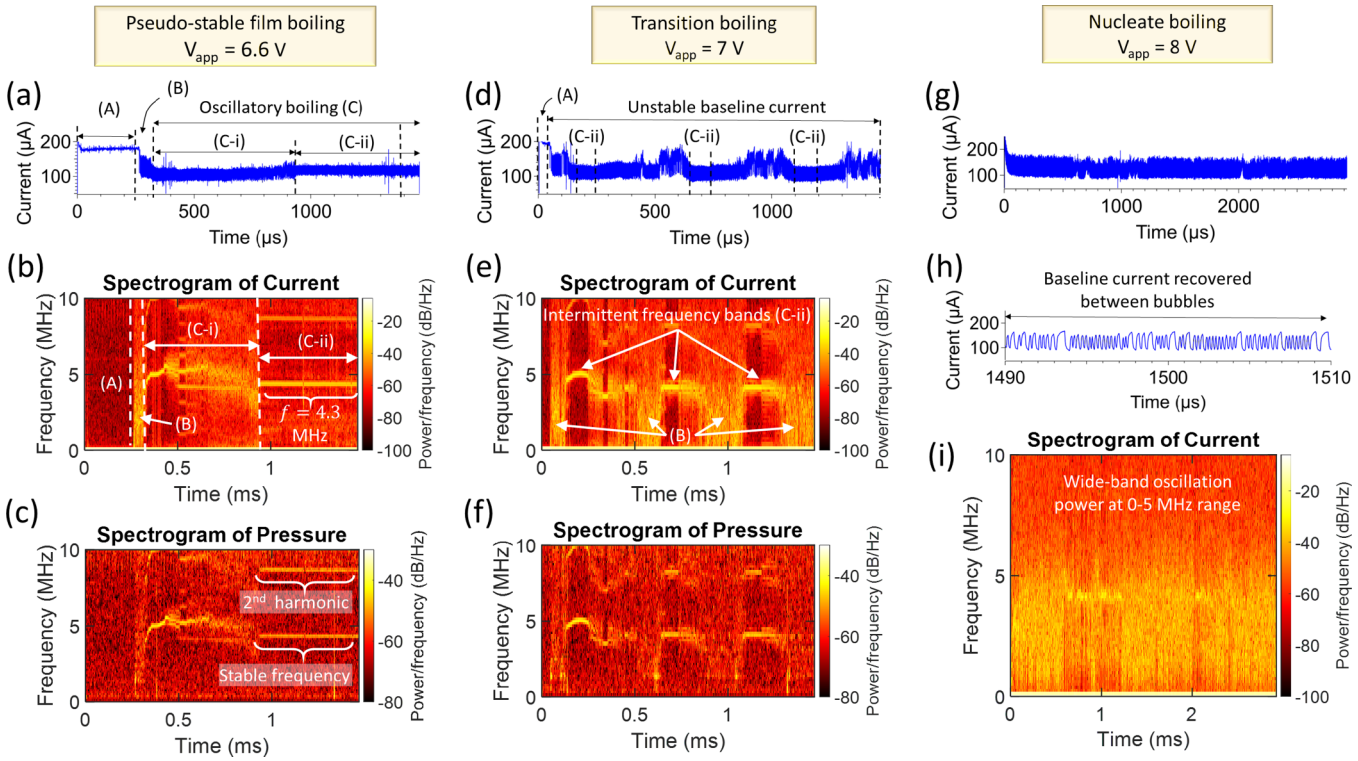

FIG. 6. Boiling transition with increasing bias voltage for a $D_p = 460$ nm pore. (a) Transient current, (b) current spectrogram, and (c) hydrophone pressure spectrogram during stable oscillatory film boiling at 6.6 V. (d) Transient current, (e) current spectrogram, and (f) hydrophone pressure spectrogram during transition boiling at 7 V. (g) Transient current of the whole voltage pulse and (h) a zoomed view during nucleate boiling at 8 V. (i) Current spectrogram at 8 V. Owing to stochastic nucleation, no clear band is seen, but high oscillation power can be seen in the 0–5 MHz range.

of a hemispherical microbubble became nonlinear and eventually unstable.

C. Film-to-nucleate boiling transition

As the torus bubble forms on the pore circumference [Fig. 1(c)(iii)], its volume scales linearly with the pore diameter, $V_b \propto D_p$, while the cylindrical pore volume where the Joule heat is generated scales quadratically, $V_p \propto D_p^2$. Thus, for torus bubbles forming on the same pore length L [Fig. 1(c)(iii)], with increasing D_p, more Joule heat will be liberated within the pore volume than can be blocked by the bubble through the volume exclusion effect. Hence, according to our hypothesis, the torus bubble will be forced to bulge outward, triggering instability and eventually a reverse transition. Through our experiments, we have found this transition to manifest in the pore diameter range of 400–500 nm. We therefore chose the 460-nm pore results to showcase the boiling structure during this process.

First, compared with the 420-nm pore at 6.3 V, which has a 700 μs duration of homogeneous nucleate boiling, the 460-nm pore at 6.6 V has a much shorter nucleate boiling zone of less than 100 μs [zone B in Fig. 6(a)]. Additionally, for the 460-nm pore, a much higher rate of patch heterogeneous nucleation is observed, owing to the lower cross-pore temperature difference ΔT_p corresponding to a given wall temperature T_w. With increasing pore diameter, the specific Joule heat density within the pore volume decreases as the pore volume offers less electrical resistance than the access region [67]. This decreases the temperature gradient from the pore center to the pore walls [39], resulting in a lower ΔT_p.

Owing to uncertainty in the heterogeneous nucleation temperature [23], the waiting times between bubble nucleations are stochastic, leading to nonperiodic bubble signals in the nucleate boiling regime, as shown in Fig. 1(c). Consequently, in zone B, a wide or nonspecific frequency band (0–5 MHz) is noticeable in the current and pressure spectrograms [Fig. 6(b)]. Each blockage signal in this zone indicates a separate bubble event comprising bubble nucleation, inertial and evaporation-induced growth to several micrometers, and eventual collapse back to the liquid phase owing to the lack of sufficient sensible heat supply. The baseline current is recovered after each bubble collapse. Owing to the abundant heterogeneous nucleation inside the 460-nm pore, the probability of eventual coalescence of patch nuclei toward formation of a film-like torus bubble on the pore surface is increased compared with the 420-nm pore. As a result, zone B is short lived, and is followed by zone C-i at 6.6 V.

The film-to-nucleate boiling transition is activated at higher bias voltages and is best captured at 7 V. As the voltage is increased from 6.6 V to 7 V, a steady and pseudostable oscillating torus bubble is never seen, as is evident from the continuously varying baseline current [Fig. 6(d)]. Also, the spectrograms reveal intermittent narrow frequency bands (C-ii) separated by unstable torus oscillations (C-i) and nucleate boiling (B) [Fig. 6(e)]. This signifies that the torus bubble is

only temporarily stable, and boiling switches chaotically [68] between nucleate boiling and film boiling multiple times. This effect is similar to the intermittent film boiling seen during transition pool boiling before the Leidenfrost point. From the first work by Nukiyama onward, much attention has been paid to intermittent film boiling, but an overall model has yet to be established [69]. Actually, for many years, the sudden dip in the boiling curve from the critical heat flux (CHF) until the Leidenfrost point was generally represented by a dashed and broken line rather than a well-characterized continuous curve [7]. In this paper, we show that by precisely controlling the bias voltage and capturing fast current transitions with a high-bandwidth oscilloscope, this region can now be characterized in minute detail.

A further increase in the bias voltage to 8 V reveals the strange phenomenon of nanopore boiling reverting to completely nucleate boiling. Figures 6(g) and 6(h) reveal a recovery in the baseline current between discrete blockage signals, and the spectrogram in Fig. 6(i) reveals wide-band oscillation power at 0–5 MHz range akin to the nucleate boiling regime (A) in Figs. 6(b) and 6(e). The reverse transition (film-to-nucleate) with increasing bias voltage is because of a higher Joule heat generation rate, which destabilizes the torus bubble, causing it to collapse. It should be noted that thermal/vapor bubbles are always in unstable equilibrium [19], and oscillations are stable only for small-amplitude driving forces [70].

As the total Joule heat generation within the pore also scales with the pore diameter, it can be expected that at a given voltage, the torus bubble will be more stable for smaller pore diameters. This can be observed by comparing the spectrograms for the 460-nm pore at 7 V [Fig. 6(e)] with those for the 340-nm pore at 7 V (Fig. S16c in the Supplemental Material [49]). While the 460-nm pore exhibits intermittent boiling at this voltage, the 340-nm pore exhibits stable film boiling at ∼15 MHz for more than 2 ms. Also, we can compare Fig. S13(b) [49], which shows the spectrogram for an expanded 250-nm pore under 7 V. Steady frequency bands in the 10 MHz range are observed. Because the experiments were repeated multiple times, the pore expanded from its initial size of 250 nm to the 300–400 nm range owing to erosion caused by nanobubble vibrations.

In the Supplemental Material [49], we examine the long-term stability of the torus bubble inside the 460-nm pore at 6.3 V and 6.5 V (see Figs. S17 and S18, respectively). We find that the 6.3 V torus bubble underwent highly nonlinear oscillations, with many subharmonic and superharmonic frequency bands. In the case of 6.5 V, the torus bubble oscillated weakly nonlinearly for ∼400 μs, before returning to nonspecific frequency bands indicative of its instability. Although we do not exactly understand the nonlinear behavior of these bubbles, we can still safely infer that for the 460-nm pore, the torus bubble is either pseudostable or unstable. Comparing the baseline current dip ratio $\Delta I_b/I_b$ during stable film boiling [Fig. 7(b)], we find that the 340-nm pore has a larger ratio than the 420-nm pore, while the 460-nm pores have nearly the same ratio as the 420-nm pore. This can be explained by comparing the volume exclusion ratios f_v of the torus bubble inside the three pore diameters. As the dip in baseline current is proportional to the volume exclusion effect posed by the torus bubble, we can expect that $f_v \propto \Delta I_b/I_b$. As shown

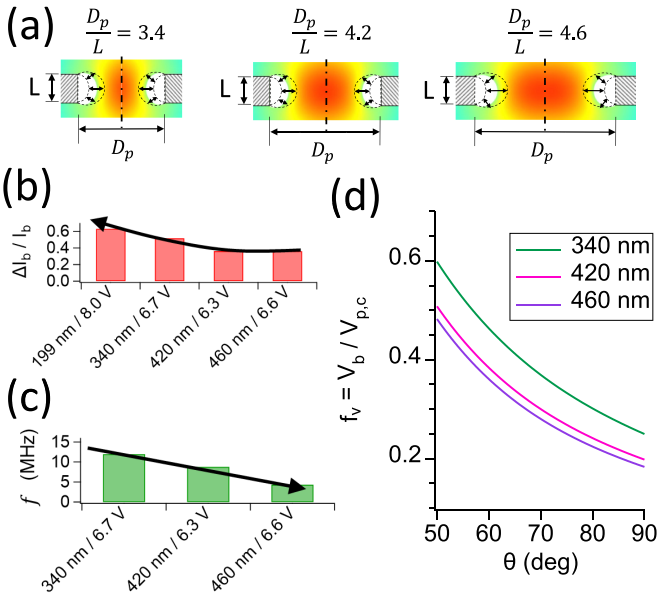

FIG. 7. (a) Schematic showing a torus bubble within a nanopore for pore diameters of 340 nm, 420 nm, and 460 nm. (b) Current baseline dip ratio $\Delta I_b/I_b$ and (c) first-harmonic frequency of stable or pseudostable torus bubble oscillations as seen in experiments for the three pore diameters. (d) Variation of the volume exclusion ratio $f_v = V_b/V_{p,c}$ with contact angle for the three pore diameters. V_b is the volume of the torus bubble and $V_{p,c}$ is the cylindrical pore volume as shown in Fig. 9(a).

in Fig. 7(d), $f_v(340\,\text{nm}) > f_v(420\,\text{nm}) \approx f_v(460\,\text{nm})$. This is responsible for the current dip ratio trend shown in Fig. 7(b). Also, the fundamental frequency of the bubble is observed to increase with decreasing pore diameter [Fig. 7(c)]. As the oscillating bubble takes a torus shape, its volume V_b will be directly proportional to the pore diameter, which will cause the frequency f to vary inversely with diameter, since frequency scales inversely to volume according to [59]. The scaling relationship of f_v with D_p also supports our hypothesis that the steady-state oscillations seen in the current and pressure spectrograms are due to a torus bubble instead of a patch bubble. In Sec. IV B, we discuss the underlying mechanism of torus bubble instability under a confined heating and pinning effect using a theoretical model. The effects of pore diameter and bias voltage on stability are also elucidated.

IV. DISCUSSION

A. Heat generation during nanopore boiling

In the previous section, nucleate boiling, transition boiling, and film boiling were categorized and analyzed minutely within each voltage pulse by deciphering changes in baseline current and oscillation frequency. As the bubble volume, pore volume, and heating volume are all comparable, the presence of a bubble inside the pore severely restricts Joule heat generation. In this section, we report the effect of the nanopore boiling regime on the heat generation rate. This effect is similar to pool boiling, where the transition to film boiling reduces the heat flux at the solid surface by cutting off liquid contact from the solid wall. However, the critical advantage

TABLE I. Variation of Joule heat generation during boiling regimes.

		Zone A		Zone B		Zone C-i		Zone C-ii	
D_p (nm)	V_{app} (V)	t_z (μs)	H (μW)	t_z (μs)	H (μW)	t_z (μs)	H (μW)	t_z (μs)	H (μW)
420	6.3	261	758	239	710	0	0	0	0
	6.4	205	772	116	669	65	484	114	517
460	6.6	263	1187	50	900	627	725	525	777
	7.0	44	1389	614	984	510	822	297	789

of studying nanopore boiling is that it allows us to focus on a single nucleation site, which is not possible in the case of pool boiling, where heat transfer properties are spatially averaged over multiple nucleation spots. Another advantage of nanopore boiling is that it allows us to investigate the transient effect of boiling transitions, thus highlighting the nonequilibrium states lying between nucleate boiling and stable film boiling. This property is specifically useful in understanding intermittent film boiling during transition boiling, an area of profound scientific interest since the work of Nukiyama.

Table I shows the average Joule heating rate $H = V_{app}I$ in different boiling zones for a single-voltage pulse of duration t_p. t_z denotes the total duration of each zone during the pulse. For the 420-nm and 460-nm pores, t_p is taken as 500 μs and 1468 μs, respectively. The 420-nm and 460-nm pore results were captured using the passive and active probes, respectively.

Some clear trends can be seen in Table I. For example, the duration of the initial heating zone (A) becomes shorter with higher voltage, signifying a more rapid temperature rise to nucleation conditions. Compared with the regime in zone A, H decreases during the nucleate boiling (B) and film boiling (C) regimes, with the latter exhibiting a greater decrease. For the 420-nm pore, during nucleate boiling (B), H is higher at 6.3 V than at 6.4 V. This is because the periodicity of bubble nucleation increases, i.e., the waiting times decrease, with increasing bias voltage, leading to more ionic current blockages. In the case of the 460-nm pore, we find that the duration of the nucleate boiling zone (B) is significantly longer at 7 V than at 6.6 V, because nucleate boiling regimes (B) appear repeatedly, suggesting the start of transition boiling. For the same reason, the duration of stable film boiling (C-ii) becomes shorter with increasing voltage. H increases by 17% in zone A, but by only 1.5% in zone C-ii. This is due to the volume exclusion effect imposed by the torus bubble.

B. Nanotorus bubble at quasi-equilibrium

In Sec. III B, we showed that in zone C-ii, steady-state current oscillations are seen with respect to a stable yet reduced baseline. The reduction in baseline current was attributed to the formation of a pseudostable torus bubble with oscillation amplitude proportional to the volumetric oscillation amplitude of the bubble. The bubble volume oscillations are due to contact angle oscillations about a mean contact angle, which are described in Appendix D. We assume the bubble to exist in a pinned state, as a result of which decreasing the contact angle causes an increase in bubble volume, and vice versa [Fig. 7(d)]. In this subsection, we model the mean torus bubble size inside the 420-nm pore by matching the experimental steady-state current in zone C-ii with steady-state Joule heating simulations.

When a torus bubble is introduced on the cylindrical silicon nitride pore surface as shown in Figs. 8 and 9(a), the Joule heat density in the liquid increases, while the total Joule heat production decreases, because of the volume exclusion effect. The torus bubble shape is calculated (Appendix A) assuming that it has a constant mean surface curvature (CMC) and that it remains pinned on the two pore edges as shown in Fig. 8. The vapor molecules inside the torus bubble transport heat between the liquid/vapor and solid/vapor interfaces (the axisymmetric view in Fig. 8), and this takes place ballistically, with no or minor intermolecular collisions [71,72]. The ballistic heat flux for a given temperature drop is much stronger and faster than continuum heat transport in the liquid [Eqs. (B6) in Appendix B]. Hence, the torus bubble offers no thermal resistance to heat transfer between the liquid/vapor and solid/vapor interfaces. We solve the energy conservation equations [Eqs. (B1) in Appendix B] in the electrolyte and the silicon nitride membrane, taking into account the Joule heat source term $\mathbf{J}\cdot\mathbf{E} \approx \sigma|\mathbf{E}|^2$, where σ, $\mathbf{J}$, and $\mathbf{E}$ are the electrical conductivity, ion flux density, and electric field, respectively. When the heat generation inside the pore and the heat diffusion through the membrane are balanced [Eqs. (B5) and Fig. 8], the steady-state nanopore and bubble

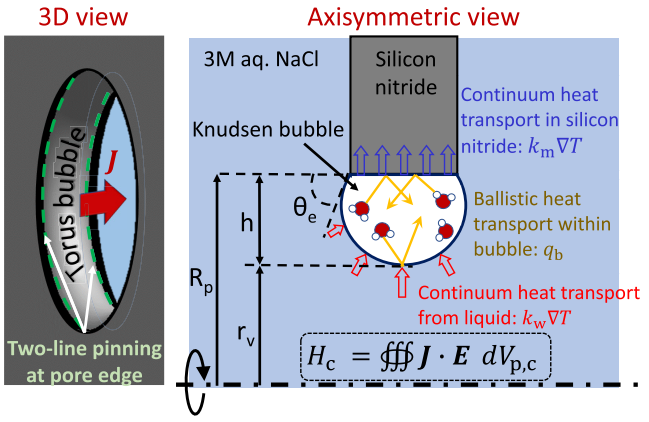

FIG. 8. Schematic explanation of the heat transfer mechanism through the torus bubble sandwiched between the Joule heated liquid and the silicon nitride membrane, which acts like a heat sink. The ion flux $\mathbf{J}$ through the unrestricted pore volume generates Joule heat H_c, part of which is transferred through the torus bubble to the silicon nitride walls. Continuum heat transport takes place in the liquid and solid, while ballistic heat transport takes place through the bubble, where the mean free path of vapor molecules is of the same order of magnitude as the bubble height h.

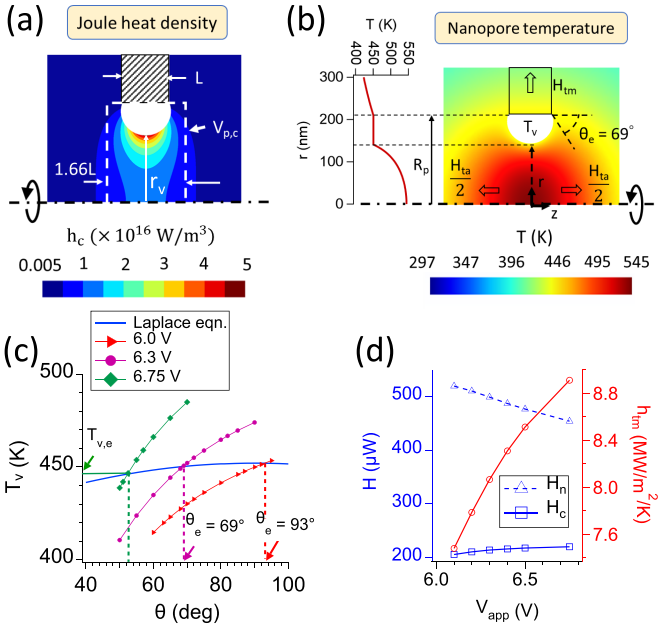

FIG. 9. (a) Steady-state Joule heat density and (b) contour plot of the steady-state temperature distribution for a 420-nm pore under 6.3 V with a $\theta = 69^\circ$ torus bubble sitting on top of $L = 100$ nm thick silicon nitride membrane walls. The temperature distribution along the bubble midline r_v is shown on the left of (b). (c) Variation of bubble temperature with contact angle under thermal steady-state conditions (lines with markers). The solid-blue line shows the variation of bubble temperature under mechanical (Laplace) equilibrium conditions. Solution of the thermal and mechanical equilibrium conditions give the overall equilibrium bubble contact angle θ_e. (d) Variation of the net Joule heat generation H_n, the Joule heat generation H_c inside $V_{p,c}$, and the heat transfer coefficients of the membrane h_{tm} when a torus bubble with equilibrium contact angle θ_e occupies the pore volume.

temperatures are obtained [Fig. 9(b)]. In this configuration, the bubble has a vapor temperature $T_v = 450.2$ K. The net Joule heat production, H_n is the sum total of the heat generation in the cylindrical pore region around the bubble [H_c inside $V_{p,c}$, shown in Fig. 9(a)] and the heat generation in the access region away from the bubble (H_a), i.e., $H_n = H_c + H_a$. For $\theta_e = 69^\circ$, as shown in Fig. 9(b), $H_n = 499\,\mu$W, $H_c = 214\,\mu$W, and $H_a = 283\ \mu$W. H_c is balanced by the diffusive heat flux through the liquid surrounding the pore ($H_{ta} = 52\ \mu$W) and the diffusive heat flux through the silicon nitride membrane ($H_{tm} = 162\ \mu$W). It should be noted that the majority of the Joule heat ($\upsilon = H_{tm}/H_c = 0.76$ or 76%) produced within the cylindrical pore region is consumed by the bubble and transferred to the silicon nitride surface on top of which it sits. Also, $H_{tm} = h_{tm} 2\pi R_p L(T_v - T_0)$, which can be solved to obtain the heat transfer coefficient of the membrane at $V_{app} = 6.3$ V, namely, $h_{tm} = 8.06$ MW m^{-2} K^{-1} [Fig. 9(d)].

Figure 9(c) shows the variation of torus bubble temperature with contact angle according to mechanical equilibrium (blue line) and thermal steady-state conditions (lines with markers) for different voltages. The vapor temperature for mechanical equilibrium has been obtained according to Eq. (C1) in Appendix C, assuming saturated vapor pressure inside the bubble, which is balanced by the Laplace pressure. In the thermal steady state, there is no heat accumulation in the bubble, and also there exists no temperature drop across the interface to cause a net evaporation flux [Eqs. (B5)]. We can see that for a given voltage, there is only one solution for the contact angle at which both mechanical equilibrium and steady-state conditions are simultaneously satisfied, namely, $\theta_e = 69^\circ$ when $V_{app} = 6.3$ V. This steady-state size and temperature of the bubble can also be termed a quasi-equilibrium state [71]. It should be noted here that the growth–collapse cycle of nucleate bubble (either homogeneous or heterogeneous) is a highly transient and out-of equilibrium process [35], and the torus film bubble can reach a quasi-equilibrium state that is experimentally observed to be stable for longer than 100 μs. This is due to the high volume of the torus bubble, which restricts Joule heat production within the pore and arrests the transient liquid temperature rise, enabling a thermal steady state to exist. It is interesting to note that at $\theta_e = 69^\circ$, the nanopore current from the simulations (Fig. S8b [49]) and the mean oscillation current observed experimentally ($I_{b,a,e,Q}$ in Fig. S19c [49]) are in agreement with each other. This justifies the attribution of the baseline current dip to the amount of volume occlusion in the pore volume provided by the torus bubble.

It should also be noted that with increasing voltage, the equilibrium temperature of the bubble $T_{v,e}$ remains almost constant, while the pinned bubble grows (i.e., θ_e decreases) significantly. Because of the negative curvature of the pore surface and the pinning effect, the curvature of the torus bubble is less sensitive to decreasing contact angle (pinned expansion, see Fig. S5c [49]), as a result of which the vapor temperature as given by the Laplace equation remains quasi-uniform. Also, the heat transfer capacity of the silicon nitride membrane is limited, which forces the bubble to grow to the limit H_c such that a thermal steady state can be established. This can be explicitly observed in Fig. 9(d), where for $\theta = \theta_e$, the net Joule heat generation H_n decreases while H_c increases slightly with increasing bias voltage. Qualitatively, this finding supports our experimental results presented in Table I, where increasing the voltage from 6.6 V to 7 V caused H to rise by only 1.5% in zone C-ii. This analysis shows that, similar to vapor films in pool boiling, which impede the solid-to-liquid heat flux, nanopore torus bubbles also exert a limiting effect, but on Joule heat generation in the bulk liquid, through volume exclusion. As Joule heating is restricted by the torus bubble, the pore center temperature is unable to rise to 600 K, thereby preventing homogeneous nucleation.

C. Stability of nanotorus bubble

Using nanopore Joule heating, we reduced the boiling scale to the 100-nm range, thus entering the domain of single-bubble dynamics. At this scale, buoyancy become insignificant, while surface tension dominates, as characterized by the very low Bond number $\mathrm{Bo} = \rho_w g R^2/\gamma = \mathcal{O}(10^{-9})$. Also, hydrodynamic instabilities can be ruled out at this scale, since the critical wavelengths for surface waves according to Rayleigh–Taylor ($\lambda_c = 14$ cm) and Kelvin–Helmholtz ($\lambda_c = 2.3$ mm) instabilities [73] are four orders of magnitude larger than the dimensions of the bubble. For Kelvin–Helmholtz

instability, we have assumed zero vapor velocity ($u_v = 0$) because of the pinning effect, while we have assumed the velocity of the liquid surrounding the bubble to be equal to the typical electro-osmotic flow velocity inside the nanopore, $u_l = 5$ m/s [74].

Instead, oscillations of the contact angle of the bubble under contact-line pinning are assumed to explain the steady-state spectrograms seen in experiments. This assumption is based on Lohse and Zhang's analytical model [45,75] and the molecular dynamics simulations by Liu *et al.* [76], where it was postulated that contact line (l = constant) pinned nanobubbles with contact angle oscillations are in stable equilibrium, while unpinned nanobubbles at fixed contact angle (θ = constant) are in unstable equilibrium. However, the dynamic equilibrium theory [77,78] suggests that a combination of contact angle motion and contact line motion [77–79] under partial pinning can also lead to stabilization. However, experimentally, there are conflicting reports on the magnitude and direction of contact line tension [79–81], and the exact θ–l correlation and its driving mechanism is still an open question. Although these complex mechanisms are possible, we model our bubble behaviors based on the simplest case of a fully pinned contact line on the pore edge ($l = L$ = constant). This is supported by several studies [36,37,43] that have visualized contact angle oscillations of microscale thermal bubbles, pinned at the edge of the heater surface.

We judge the stability of thermal bubble equilibrium from first principles, by perturbing the bubble slightly and checking whether there is a positive restoring force [70,82]. Hence, when a thermal bubble initially in quasi-equilibrium is radially perturbed (ΔR), the restoring force F can be written as

$$F = S_b \Delta(P_v - P_w - K\gamma) = -\kappa \Delta R. \tag{2}$$

Here, K and S_b are the curvature and liquid/vapor interfacial surface area of the bubble, respectively (Fig. S5 [49]). κ is the mechanical stiffness, which must satisfy $\kappa > 0$ for stable equilibrium. P_v and γ are the vapor pressure and surface tension, respectively, of water at saturation temperature. P_w is the atmospheric pressure. It should be noted that submicrometer-scale thermal spherical bubbles are regarded to be in unstable equilibrium [19]. For a spherical vapor bubble with radius R_e and temperature T_v in mechanical and thermal equilibrium in an infinite reservoir, the linear oscillation model, Eq. (2), can be written as [82]

$$\rho_w R_e \omega^2 = \frac{h_{fg}\rho_v}{\rho_w c_w T_v}\sqrt{\frac{\omega}{2D_{th}}} - \frac{2\gamma}{R_e^2}, \tag{3}$$

with $\kappa = \mathcal{M}\omega^2$, where $\mathcal{M} = 4\pi\rho_w R_e^3$ is the reduced mass of radial oscillations of a spherical bubble [83,84]. There exists a real solution for ω only when $R_e \geqslant 14\,\mu$m. This is due to the inverse relation between curvature and bubble radius, $K = 2/R$, which causes the surface tension force to dominate for smaller bubbles, leading to $\kappa < 0$ and preventing stable equilibrium. This analysis, however, begs the question: how does a $\mathcal{O}(100\,\text{nm})$ torus bubble attain stability within the nanopore, making stable film boiling possible in the first place.

Next, we judge the thermal stability of the torus bubble equilibrium. Assuming that thermal equilibrium is maintained at the liquid–vapor and solid–vapor interfaces, (T_v=T_w=T_m) and that the vapor temperature varies along the saturation line ($\Delta P_v/\Delta T_v = h_{fg}\rho_v/T_v$) [70], Eq. (2) can also be written as

$$\kappa = -\frac{S_b^2}{\psi}\left(\frac{h_{fg}\rho_v}{T_v}\cos\delta - \psi\gamma\frac{dK}{dV_b}\right)$$
$$= S_b^2\left(\eta_2 - \frac{h_{fg}\rho_v}{T_v}\frac{\cos\delta}{\psi}\right) = \mathcal{M}(\theta_e)\omega^2. \tag{4}$$

Here, $\mathcal{M}(\theta_e)$ is the reduced mass of contact angle oscillations of the pinned torus bubble with quasi-equilibrium contact angle θ_e. A detailed derivation is provided in Appendix D [Eqs. (D1)–(D10)]. h_{fg} and ρ_v are the latent heat and vapor density, respectively, assuming saturation conditions. For linear oscillations of the bubble volume V_b and temperature T_v given by $V_b = V_{b,e} + V_{b,a}\exp(j\omega t)$ and $T_v = T_{v,e} + T_{v,a}\exp[j(\omega t + \delta)]$, with $j = \sqrt{-1}$, $\psi = V_{b,a}/T_{v,a}$ denotes the volume expansion coefficient (i.e., the ratio of volume and temperature amplitudes) and δ ($-90^\circ \leqslant \delta \leqslant 90^\circ$) denotes the phase difference between them. η_2 is the curvature coefficient capturing the variation of bubble curvature with contact angle for a given pore size, as shown in Fig. S6 [49].

Thus, for stable equilibrium, the mechanical stiffness of the bubble must satisfy $\kappa > 0$, which necessitates that there be a positive restoring force responsible for returning the bubble back to equilibrium conditions after it has been perturbed. As the bubble expands, the Joule heat density inside the pore increases ($d\hat{h}_c/d\theta < 0$ in Fig. S8c [49]). This rise in heat generation is balanced by the internal energy rise of the system, the latent heat of evaporation into the bubble, the P–V work done by the bubble, and the rise in heat flux from the bubble to the silicon nitride membrane [Eq. (D3) in Appendix D]. Thus, by perturbing the energy balance of the bubble, ψ and δ are obtained. Excess heat generation leads to $\psi > 0$. On the other hand, if the bubble expansion consumes more heat than is being generated, then $\psi < 0$.

Figure 10 summarizes the four stability parameters η_2, ψ, δ, and κ for the equilibrium torus bubble inside the 420-nm pore. Owing to the pinning effect, the curvature perturbation $\eta_2 \geqslant 0$ for $\theta_e \geqslant 90^\circ$, which causes κ to increase [Eq. (4)], providing a positive restoring force following volume perturbation. In this θ range, at the high-frequency limit where $\psi < 0$, temperature perturbations will also tend to increase κ, thus lending an extra stabilization effect. Owing to the dual effect of curvature stability ($\eta_2 > 0$) and thermal stability ($\psi < 0$), nanotorus film bubbles inside a nanopore can exist in stable equilibrium. This behavior is, however, not possible for spherical bubbles at the same scale.

However, when $\psi > 0$ [Fig. 10(b)] and $|\delta| < 90^\circ$ in the low-frequency range [Fig. 10(c)], the thermal perturbation

$$-\frac{h_{fg}\rho_v}{T_v}\frac{\cos\delta}{\psi}$$

becomes negative and can overpower the curvature stability, triggering destabilization. This can be seen for the κ trace [Fig. 10(d)] at 6.0 V, which enters the stable equilibrium zone ($\kappa > 0$) only beyond a critical frequency (3 MHz). In the stable equilibrium zone, the solution for κ according to Eq. (4) (solid line) and $\kappa = \mathcal{M}\omega^2$ [dashed line in Fig. 10(d)] gives a resonant frequency $f = 20.8$ MHz for the 93°torus bubble at

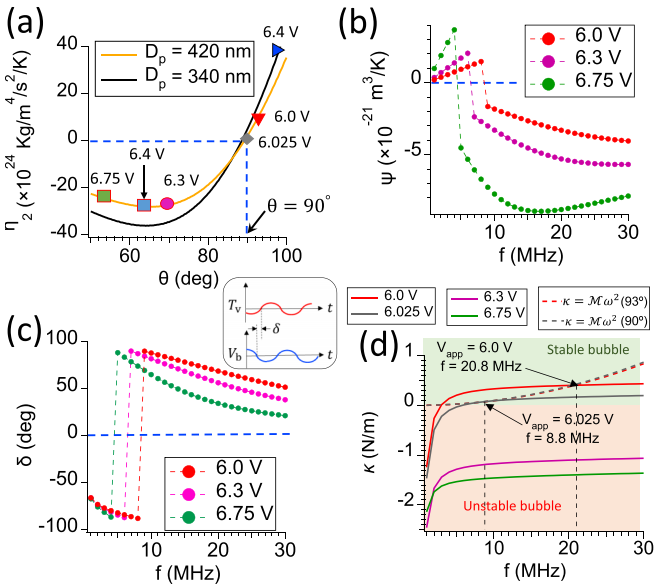

FIG. 10. Variation of torus bubble stability parameters with oscillation frequency f under different bias voltages V_{app}: (a) curvature coefficient η_2; (b) volume expansion coefficient ψ; (c) phase difference δ between bubble temperature and volume; and (d) mechanical stiffness κ for the 420 nm pore.

6.0 V and $f = 8.8$ MHz for the 90° torus bubble at 6.025 V. Here, $\omega = 2\pi f$ is the angular frequency and $\mathcal{M} = 2.23 \times 10^{-17}$ kg is the reduced mass for the 93° torus bubble inside the 420-nm pore. The method for calculating the reduced mass numerically is described in Appendix E [Eq. (E3)]. By comparison, in experiments, we observed a stable oscillation frequency of 8.9 MHz for the 420-nm pore at 6.3 V. Compared with the 93° torus, the curvature coefficient η_2 is smaller for the 90° torus, leading to a smaller stiffness and resonant frequency. Again, for $\theta < 90°$, η_2 decreases, leading to bubble instability. Hence, we can say that $f = 8.8$ MHz is the minimum frequency for stable torus oscillations. It should also be noted that at $\theta_e = 90°$, the curves of $\kappa = \mathcal{M}\omega^2$ and Eq. (4) are tangent to each other. Also, at this limit where the modeled and experimental resonant frequencies match, the error of ~0.3 V is acceptable given the approximations in our model. We should also cite the analytical model by Dockar *et al.* [59], which was formulated for adiabatic bubble oscillations on a flat surface. According to that model, the natural frequency of a 90°patch heterogeneous bubble pinned on a 100-nm flat surface is in the region of 450 MHz. The one order smaller frequency for the torus bubble observed here is due to (i) a larger volume compared with a patch bubble, which leads to a larger reduced mass $\mathcal{M}$, and (ii) lower stiffness and smaller volume expansion coefficient magnitude $|\psi|$ owing to Joule heat density amplification with bubble enlargement.

However, with increasing bias voltage, the equilibrium bubble volume increases (i.e., θ_e decreases), which causes the bubble to enter the $\eta_2 < 0$ zone, where the surface tension force tends to reduce κ. This can be observed in Fig. 10(a), where for 6.0 V, $\eta_2 > 0$, but for 6.3 V and 6.75 V, $\eta_2 < 0$. In this range, even for $\psi < 0$ and $\delta \to 0°$, a positive κ is not obtained, and thus the torus bubble equilibrium is unstable. This trend is supported by our experiments, where with increasing voltage, the stable torus bubble zone (C-ii) decreases in extent and eventually disappears, paving the way toward transition back to nucleate boiling.

This theory also explains the higher stability of torus bubble films with decreasing pore size. As shown in Fig. 10(a), for the 340-nm pore, a bias voltage of 6.4 V results in an equilibrium torus bubble contact angle in the $\theta_e > 90°$range, where curvature perturbation enhances bubble stability ($\eta_2 > 0$). As the heat transfer capacity of the silicon nitride membrane (h_{tm}) is limited, the bubble volume will increase to the limit H_c with increasing voltage, and so a thermal steady state will be achieved. Therefore, smaller pore diameters, which have a higher bubble volume exclusion ratio [f_v in Fig. 7(d)] for the same θ, allow a thermal steady state to be established at $\theta_e \to 90°$or $\theta_e > 90°$. This indicates that stable film boiling will persist to higher voltages as the pore diameter is decreased. Our experiments also support this hypothesis, where stable film boiling exists for 6.7 V and 7 V for the 340-nm pore, whereas for the 420-nm pore, loss of stable film boiling is triggered at 6.5 V.

It should be noted that this model only checks stability in the quasi-equilibrium state of the bubble. To avoid the zone of curvature instability ($\theta_e < 90°$), the mean bubble size may exist in an out-of-equilibrium state, with $\theta_e \approx 90°$, where it can be quasistable with nonlinear and large-amplitude oscillations as seen in experimental spectrograms. The linear model described here is also not able to capture the complex out-of-equilibrium behavior of the torus bubble, when the bubble destabilizes probably through Laplace pressure bubble catastrophe [58] or loss of contact line pinning [75] and a complete multiphase computational fluid dynamics (CFD) treatment may be necessary.

V. CONCLUSIONS

In summary, we have presented a consolidated picture of boiling inside a cylindrical nanopore, which differs significantly from traditional pool boiling owing to the confined nature of Joule heat generation and bubble dynamics. Measuring the ionic current flow reduction with bubble formation within the nanopore volume and stress waves generated by bubble motion enable investigation of vapor nanobubbles at nanosecond resolution. Two contrasting modes of boiling are detected: (i) nucleate boiling inside the nanopore, involving discrete homogeneous and patch heterogeneous bubble nucleation with explosive growth and collapse cycles, and (ii) oscillatory film boiling, involving a torus bubble that can undergo steady-state oscillations in resonance with Joule heating, while preventing nucleate boiling at the same time. Interestingly, with increasing bias voltage, a reverse transition from film to nucleate boiling is observed. The dynamics of the torus bubble are explained with the help of theoretical models. Owing to the pinning effect, the torus bubble, albeit at the nanoscale, is able to attain a stable equilibrium in the low-bias-voltage range. However, with increasing voltage, the labile vapor bubble expands in a pinned state to limit Joule heat generation and establish quasithermal equilibrium. However, the mechanical stiffness of the bubble decreases with increasing volume, and beyond a critical voltage, the

stiffness becomes negative, making the equilibrium unstable and ultimately destabilizing the torus bubble.

ACKNOWLEDGMENTS

This work was supported by JSPS KAKENHI Grants No. JP20H02081 and No. JP20J22422. A part of this work was conducted at Advanced Characterization Nanotechnology Platform of the University of Tokyo, supported by "Nanotechnology Platform" of the Ministry of Education, Culture, Sports, Science and Technology (MEXT), Japan.

APPENDIX A: TORUS BUBBLE SHAPE CALCULATIONS

Assuming that the torus bubble has uniform mean curvature K, this can be expressed as [85]

$$K = \frac{b' \sin\nu + b\cos\nu}{(a + b\cos\nu)\sqrt{b^2 + b'^2}} - \frac{bb'' - 2b'^2 - b^2}{(b^2 + b'^2)\sqrt{b^2 + b'^2}}, \quad \text{(A1)}$$

where b is the radial distance from the first-principal center of curvature, which varies with ν. Thus, $b' = db/d\nu$. From symmetry, we know that $b' = 0$ when $\nu = 180^\circ$. Let the value of b at $\nu = 180^\circ$ be b_π. Now, for a given value of K, we can solve for b'', which we can use to incrementally obtain b and b' for decreasing values of ν from $\nu = 180^\circ$ to $\nu = 0^\circ$, thus tracing the constant-mean-curvature (CMC) torus bubble interface. Mathematically,

$$\begin{aligned} b'(\nu + \Delta\nu) &= b'(\nu) + b''(\nu)\Delta\nu, \\ b(\nu + \Delta\nu) &= b(\nu) + b'(\nu + \Delta\nu)\Delta\nu, \end{aligned} \quad \text{(A2)}$$

where $\Delta\nu = -0.0018^\circ$. We find that only when $K = (a - 2b_\pi)/[b_\pi(a - b_\pi)]$ is the torus bubble surface free of perturbations and the surface area is minimized. Now, for different values of $[a, b_\pi]$, $[K, l, \theta]$ are calculated. Here, l is the bubble length on the pore surface and θ is the contact angle, as shown in Fig. S5(a) in the Supplemental Material [49]. The values of $[a, b_\pi]$ that satisfy the pinning condition $l = L$ are selected, and geometric properties such as the bubble volume V_b and surface area S_b are obtained by numerical integration over the tracer points (R, Z) used to construct the surface (Figs. S5e and S5f in the Supplemental Material [49]).

APPENDIX B: JOULE HEATING MODEL

To obtain the temperature distribution responsible for the bubble behavior, numerical simulations are employed to solve the energy-conservation equations in the liquid and the silicon nitride membrane,

$$\begin{aligned} \rho_w c_{p,w}\frac{\partial T}{\partial t} &= \frac{1}{r}\frac{\partial}{\partial r}\left(k_w r\frac{\partial T}{\partial r}\right) + \frac{\partial}{\partial z}\left(k_w\frac{\partial T}{\partial z}\right) + \sigma|\mathbf{E}|^2, \\ \rho_m c_m\frac{\partial T}{\partial t} &= \frac{1}{r}\frac{\partial}{\partial r}\left(k_m r\frac{\partial T}{\partial r}\right) + \frac{\partial}{\partial z}\left(k_m\frac{\partial T}{\partial z}\right). \end{aligned} \quad \text{(B1)}$$

Here, ρ_w, $c_{p,w}$, and k_w are the temperature-dependent water density, specific heat, and thermal conductivity, respectively [24,86], and t is time. ρ_m, c_m, and k_m are the density, specific heat, and thermal conductivity of the silicon nitride membrane. σ is the electrical conductivity of the electrolyte, which is captured using an empirical relation first established by Levine *et al.* [24],

$$\sigma = mT - b - \frac{(T - T_0)^\alpha}{\beta}, \quad \text{(B2)}$$

where $m = 0.391$ S m^{-1} K^{-1}, $b = 0.391$ S/m, $\beta = 5.6\times10^4$, and $T_0 = 293.15$ K. α is the only fitting parameter that is varied to fit the preboiling baseline current I_b of the nanopore. $\alpha = \{2.7, 2.65, 2.7\}$ for the 340-nm, 460-nm, and 1134-nm diameter pores, respectively. The electric field inside the liquid is obtained by combining the ion flux balance ($\nabla\cdot\mathbf{J} = d\rho_e/dt$) and Poisson's equation ($\nabla\cdot\epsilon\mathbf{E} = \rho_e/\varepsilon_0$),

$$\nabla\cdot(\sigma\nabla U) = \frac{d}{dt}[\varepsilon_0\nabla\cdot(\epsilon U)], \quad \text{(B3)}$$

where $\mathbf{J} = \sigma\mathbf{E}$ is the ionic flux, and U, ρ_e, ε_0, and ϵ are the electric potential, induced charge, dielectric permittivity of free space, and temperature-dependent dielectric constant of water, respectively [24,39]. The boundary conditions for T and J applied on the simulation boundaries are shown in Figs. S9(a) and S9(b) in the Supplemental Material [49].

In an axisymmetric reference frame with origin at the center of the nanopore, r represents the radial coordinate and z the axial coordinate. Equations (B1) are solved on a finite-volume mesh with appropriate boundary conditions and numerical discretizations [87] (Sec. S3 of the Supplemental Material [49]). As the nanopore temperature increases, so too does the electrolyte conductivity, allowing greater current flow for the same voltage,

$$\begin{aligned} I_b &= 2\pi\int_0^{R_p}\sigma\mathbf{E}\cdot\hat{\mathbf{z}}r\,dr, \\ I_{b,a} &= 2\pi\int_0^{r_v}\sigma\mathbf{E}\cdot\hat{\mathbf{z}}r\,dr, \end{aligned} \quad \text{(B4)}$$

where I_b denotes the baseline current development before the onset of bubble nucleation as shown by the red dashed line in Fig. S19(a) [49]. As can be seen, the experimental and simulation current development match reasonably well except for the initial 20 μsec, when membrane capacitive charging affects the nanopore current [39,88]. At the point of first homogeneous bubble nucleation, the temperature at the pore center reaches 584 K, which is the range of theoretical homogeneous nucleation temperatures [89].

Next, we apply the same model to a steady-state nanopore–bubble system where a torus bubble blankets the cylindrical pore surface, as shown in Fig. 9(b). We assume that the liquid and silicon nitride are in thermal equilibrium with the bubble temperature, i.e.,

$$\begin{aligned} T_v &= T\|_{S_b} = T\|_{S_p}, \\ \int_{S_b} k_w\nabla T\cdot\hat{\mathbf{n}}\,dS &= \int_{S_p} k_m\nabla T\cdot\hat{\mathbf{n}}\,dS, \end{aligned} \quad \text{(B5)}$$

where $\hat{\mathbf{n}}$ is the normal vector to the surface concerned, S_b denotes the liquid–vapor interface, and $S_p = 2\pi R_p L$ the vapor-solid interface. Equations (B5) signify that the vapor inside the bubble has a uniform temperature from the liquid/vapor interface to the vapor/solid interface and that the heat flux from the liquid to the bubble is balanced by the heat flux from the bubble to the silicon nitride wall on top

of which it sits. Hence, for the steady-state size, there is no heat accumulation within the bubble and no evaporative mass transfer across the interface.

The above assumptions are valid when the vapor inside the bubble is assumed to be a Knudsen gas (i.e., the Knudsen number Kn > 1) [71,90]. According to Craig [91], bubbles smaller than 100 nm typically satisfy the Knudsen gas definition. The Knudsen number is given by $\mathrm{Kn} = \lambda/h$, where $\lambda = k_B T_v/\sqrt{2}\sigma_A P_v$ is the mean free path of vapor molecules and h is the distance between the liquid/vapor and vapor/solid interfaces, as shown in Fig. 8. σ_A is the molecular cross-sectional area and k_B is Boltzmann's constant. Taking the diameter of a water molecule to be $d_w = 2.7$ Å and $\sigma_A = \pi {d_w}^2$, $\lambda = 20.6$ nm. For the bubble shown in Fig. 8, $h \sim R_p - r_v = 69$ nm, which leads to a Knudsen number $\mathrm{Kn} = 0.299$, which falls in the transition regime ($0.1 < \mathrm{Kn} < 10$). On the other hand, the collision length of liquid water molecules in the pore is 0.13 nm, which is much smaller than the pore diameter (340–460 nm). In this situation, the heat transfer in the pore liquid is governed by continuum transport. On the other hand, the heat flux through the bubble can be assumed to be governed by the ballistic heat flux according to kinetic theory (q_b), which is given by [71]

$$q_b = \alpha_c \rho_{w,n} \sqrt{\frac{2k_B^3}{m}} \left(T_{lv}^{3/2} - T_{sv}^{3/2}\right). \tag{B6}$$

Here, α_c is the accommodation coefficient, which can be assumed to be 1 [92]. m is the mass of one water molecule. $\rho_{w,n}$ is the liquid molecule number density on the liquid/vapor interface. T_{lv} and T_{sv} are the temperatures on the liquid/vapor and solid/vapor interfaces. For a Knudsen gas at $T_{lv} = 450$ K and $T_{sv} = 445$ K, $q_b = 1982.4\,\mathrm{MWm}^2$. On the other hand, the heat flux on the solid/vapor interface, $k_m \nabla T$, in Fig. 9(b) comes out to be $1227\,\mathrm{MWm}^2$. These calculations show that a mere 5-K temperature drop between the two interfaces can account for the huge heat flux through the bubble. Physically, this high heat transfer rate is possible when vapor molecules evaporating from the liquid/vapor interface at high temperature travel to and collide with the solid/vapor interface at a lower temperature without interacting with other vapor molecules inside the bubble, thereby transporting heat without creating a temperature gradient. Also, according to kinetic theory, the root-mean-square velocity of vapor molecules within the bubble, $u_v = \sqrt{3k_B T_v/m} = 788\ \mathrm{ms}^{-1}$ when the vapor temperature $T_v = 450$ K. On the other hand, the time scale of thermal relaxation in the water in the pore volume can be obtained as $\tau_w \sim D_p^2/\alpha_{th} = \mathcal{O}(100)$ ns, where $\alpha_{th} = k_w/(\rho_w c_{p,w})$ is the thermal diffusivity of water. This is of the same order as τ_ω, while the lifetime of the stable torus bubble has been observed for more than 100 μs. This fits well with our theory that the nanopore temperature distribution approaches a steady state for the mean torus bubble size.

However, in a real situation, the heat transport through the bubble will be a combination of both diffusive and ballistic transport, since the Knudsen number of the bubble is close to the Kn = 1 limit. In our model, for the sake of simplicity, we have neglected continuum diffusive transport through the bubble, assuming that the heat flux in the liquid surrounding the bubble can be balanced by the ballistic heat flux without incurring a huge temperature drop within the bubble. Thus, the vapor temperature within the bubble remains uniform and the heat flux is balanced, ensuring thermal quasi-equilibrium of the bubble. It should be noted that when this assumption is adopted, the steady-state liquid temperature distribution within the pore is such that the corresponding steady-state current $I_{b,a}$ (Fig. S8b [49]) obtained according to the second of Eqs. (B4) in Appendix B matches the experimental mean current for a steady-state torus bubble (Fig. S19c in the Supplemental Material [49]), thus justifying our model.

APPENDIX C: BUBBLE MECHANICAL EQUILIBRIUM

For net equilibrium, the torus bubble should be in mechanical equilibrium in addition to a thermal steady state, which can be quantified by the Young–Laplace equation

$$P_v = P_w + \gamma K, \tag{C1}$$

where K is the curvature of the torus bubble surface and γ is the temperature-dependent surface tension of water. Assuming chemical equilibrium between liquid and vapor, the vapor pressure of the bubble, P_v, is related to the saturation vapor pressure P_{sat} and the vapor temperature T_v according to $P_v = P_{sat} \exp[(P_w - P_{sat})M_w/(N_A \rho_w k_B T_v)]$, where P_{sat} is evaluated at T_v^*, assuming saturation conditions. Here, M_w, N_A, and k_B are the molecular weight of water, Avogadro's number, and Boltzmann's constant, respectively.

APPENDIX D: LINEAR MODEL FOR BUBBLE OSCILLATIONS

To model the thermal contact angle oscillation frequency of the torus bubble, we adopt and extend the linear and approximate model described in Hao and Prosperetti [70] and originally proposed by Alekseev [93]. We assume that the bubble contains saturated vapor and is in thermal equilibrium with the surrounding liquid and the silicon nitride membrane surface on which it sits, $T_v = T_w = T_m$. Also, for small-amplitude oscillations in contact angle, the vapor pressure inside the bubble is assumed to vary along the saturation line. So, for a change in bubble volume of ΔV_b corresponding to a contact angle change of $\Delta\theta$, the bubble mass can be expanded by applying the chain rule,

$$\Delta m_b = \rho_v \Delta V_b + V_b \Delta \rho_v = \rho_v \frac{dV_b}{d\theta}\Delta\theta + V_b \frac{d\rho_v}{dT_v}\Delta T_v, \tag{D1}$$

where ρ_v is the saturation vapor density. Here we have replaced volume perturbation by contact angle perturbation as follows: $\Delta V_b = (dV_b/d\theta)\Delta\theta$, with $dV_b/d\theta$ being obtained from Fig. 7(d). This linear expansion is accurate for small-amplitude contact angle oscillations. When there is no external heating, the increase in bubble mass is caused by the evaporation of liquid on the interface, the latent heat of which causes a reduction in interface liquid temperature by ΔT_v. Therefore,

$$-S_b \sqrt{\frac{2D_{th}}{\omega}}\, \rho_w c_w \Delta T_w = h_{fg} \Delta m_b, \tag{D2}$$

where S_b is the liquid/vapor surface area of the torus bubble. Here, h_{fg} and $D = k_w/(\rho_w c_w)$ are the latent heat and

thermal diffusion coefficient, respectively. k_w, ρ_w, and c_w are the thermal conductivity, density, and specific heat capacity of water as functions of the liquid temperature. For low-amplitude oscillations at low frequencies, it is valid to assume that the thermal equilibrium at the bubble/liquid and bubble/membrane interfaces is not lost: $\Delta T_v = \Delta T_w = \Delta T_m$. In our experiments, we find the torus film bubble to oscillate at time periods in the range of $\tau_\omega = \mathcal{O}(100)$ ns. In comparison, the ballistic heat transport through a vapor nanobubble has a time scale of $\tau_v \sim h/u_v = \mathcal{O}(0.1)$ ns. As $\tau_\omega \gg \tau_v$, it is assumed that thermal equilibrium is maintained at the bubble interfaces during oscillations. The term $\sqrt{2D_{th}/\omega}$ [19] represents the thermal relaxation length over which the temperature decrease ΔT_w is observed. Here, ω is the angular frequency of bubble oscillation. Now, in the presence of Joule heating, this energy balance equation needs to be modified to account for the additional Joule heat generation due to bubble expansion, ΔV_b, which tends to increase the temperature in the thermal relaxation length. Thus,

$$\begin{aligned}\frac{d\hat{h}_c}{dV_b}S_b\sqrt{\frac{2D_{th}}{\omega}}\Delta V_b - h_{tm}S_p\Delta T_v &= (h_{fg}\rho_v + P_v)\frac{\Delta V_b}{\Delta t} \\ &+ \left(S_b\sqrt{\frac{2D_{th}}{\omega}}\rho_w c_w + S_p\sqrt{\frac{2D_m}{\omega}}\rho_m c_m \right. \\ &\left. + h_{fg}V_b\frac{d\rho_v}{dT_v}\right)\frac{\Delta T_v}{\Delta t}, \end{aligned} \tag{D3}$$

where $S_p = 2\pi R_p L$ is the cylindrical nanopore surface area of the silicon nitride membrane and $\hat{h}_c = H_c/V_{p,c}$ is the average Joule heat density over the cylindrical pore volume $V_{p,c}$. H_c is calculated by simulating the steady-state Joule heat and temperature distributions in the presence of the torus bubble following the model described in Eqs. (B1)–(B5). $V_{p,c}$ is the cylindrical pore volume, which extends for $1.66L$ across the pore midline ($z = 0$), enclosing the torus volume V_b [Figs. 9(a) and 9(b)]. $D_m = k_m/(\rho_m c_m)$ is the thermal diffusivity of the silicon nitride membrane. As discussed in Appendix B, in the equilibrium bubble position, the net Joule heat production rate in $V_{p,c}$ is balanced by the heat dissipation through the surrounding liquid and the bubble, thereby rendering a steady-state temperature distribution.

Using Joule heating simulations, we have calculated the increase in Joule heat density $\hat{h}_c$ for different contact angles θ_e of the torus bubble during pinned expansion (Fig. S8c in the Supplemental Material [49]) and have found that for large θ_e, when the bubble expands to constrict the pore volume, the Joule heat density increases in the cylindrical pore region: $d\hat{h}_c/dV_b > 0$. This increase in heat generation is in turn balanced by a change in heat transfer through the membrane ($h_{tm}S_p\Delta T_v$), latent heat consumption by the bubble ($h_{fg}\rho_v\Delta V_b/\Delta t$), P–V work done by the bubble, and sensible heat rise in the thermal relaxation length in the liquid and the silicon nitride. Here, the internal energy rise of the bubble is neglected because of its comparatively lower heat capacity than the liquid layers surrounding it. Thus, in short, Eq. (D3) accounts for the energy balance of the bubble and the thermal boundary layers on its interfaces.

As the Eq. (D3) contains time-derivative terms, the solution for T_v oscillations will not be in the same phase as that for V_b oscillations. We can write

$$\begin{aligned}\theta &= \theta_e - \theta_a\exp(j\omega t), \\ V_b &= V_{b,e} + V_{b,a}\exp(j\omega t), \\ T_v &= T_{v,e} + T_{v,a}\exp[j(\omega t + \delta)],\end{aligned} \tag{D4}$$

where $j = \sqrt{-1}$. Here, the oscillation amplitudes of contact angle, bubble volume, and bubble temperature are taken to be positive by convention, i.e., $\theta_a > 0$, $V_{b,a} > 0$, and $T_{v,a} > 0$. δ is the phase difference between volume expansion and vapor bubble temperature rise. Substituting Eq. (D4) into Eq. (D3), we obtain

$$V_{b,a}(B - jA) = T_{v,a}\exp(j\delta)(D + jC), \tag{D5}$$

where

$$\begin{aligned}B &= \frac{d\hat{h}_c}{dV_b}S_b\sqrt{\frac{2D_{th}}{\omega}}, \quad A = \omega(h_{fg}\rho_v + P_v), \\ D &= h_{tm}S_p, \quad C = \omega\left(S_b\sqrt{\frac{2D_{th}}{\omega}}\rho_w c_w + h_{fg}V_b\frac{d\rho_v}{dT_v}\right).\end{aligned}$$

Equating the real parts and imaginary parts of Eq. (D5), we arrive at

$$\begin{aligned}\tan\delta &= \frac{AD + BC}{AC - BD}, \\ \cos\delta &= \psi\left(\frac{BD - AC}{D^2 + C^2}\right).\end{aligned} \tag{D6}$$

Because $A > 0$, $B > 0$, $C > 0$, and $D > 0$, for small positive values of δ, $\tan\delta > 0$ will be satisfied only when $AC > BD$. Here $\psi = V_{b,a}/T_{v,a}$. Now, the ratio of bubble volume amplitude and bubble temperature amplitude can be solved for from Eq. (D6) as

$$\psi = -\text{sign}(\delta)\left[\frac{D^2 + C^2}{\sqrt{(AC - BD)^2 + (AD + BC)^2}}\right]. \tag{D7}$$

It is interesting to note that when this ratio is negative, with increasing bubble volume, the vapor temperature will fall, and thus the vapor pressure inside the bubble is also expected to decrease along the saturation line $\Delta P_v = (dP/dT)_{sat}\Delta T_v = h_{fg}\rho_v/T_v\Delta T_v$. Hence, a resisting force opposing bubble expansion F is developed,

$$F = S_b\Delta(P_v - P_w - K\gamma) = -\kappa\Delta R = -\kappa\frac{\Delta V_b}{S_b}, \tag{D8}$$

i.e.,

$$S_b\left(\frac{h_{fg}\rho_v}{T_v}\Delta T_v - \gamma\frac{dK}{dV_b}\Delta V_b - K\frac{d\gamma}{dT_v}\Delta T_v\right) = -\kappa\frac{\Delta V_b}{S_b}, \tag{D9}$$

where $\Delta R = \Delta V_b/S_b$ is the expansion in bubble size. Now, substituting $\Delta V_b = V_{b,a}\exp(j\omega t)$, $\Delta T_v = T_{v,a}\exp[j(\omega t + \delta)]$, and $\psi = V_{b,a}/T_{v,a}$ into Eq. (D9) and solving for the real part,

we obtain

$$\kappa = -S_b^2\left(\frac{h_{fg}\rho_v}{\psi T_v}\cos\delta - \gamma\frac{dK}{dV_b} - K\frac{d\gamma}{dT_v}\frac{\cos\delta}{\psi}\right)$$
$$= S_b^2\left(\eta_2 - \frac{h_{fg}\rho_v}{T_v}\frac{\cos\delta}{\psi} + \eta_1\frac{\cos\delta}{\psi}\right). \quad \text{(D10)}$$

The imaginary part of Eq. (D9) would correspond to the damping term associated with temperature being out of phase with volume perturbation. Here, κ is the mechanical stiffness of the torus bubble and γ is the temperature-dependent surface tension of water. η_1 and η_2 are the curvature coefficients, which depend on the bubble curvature and in turn on contact the angle and pore size, as shown in Fig. S6 in the Supplemental Material [49]. It should be noted that $\psi\eta_2$ is an order of magnitude higher than η_1, and so variations in η_1 can be neglected for the sake of this discussion. It should be noted that we ignore the recoil force applied on the bubble interface due to evaporation/condensation. The recoil pressure, which is given by $|\dot{m}|^2(1/\rho_v - 1/\rho_w) \approx \rho_v\omega^2\Delta R^2$, is proportional to the square of the bubble radius perturbation and thus can be neglected for small-amplitude oscillations.

APPENDIX E: REDUCED MASS OF PINNED TORUS BUBBLE

Under the constraint of pinning, as a torus bubble with contact angle θ oscillates with a contact angle velocity $\dot{\theta}$, the liquid surrounding the bubble also develops a velocity according to the continuity equation. According to the definitions of the reduced or effective mass of bubble oscillations, the kinetic energy of the liquid can be expressed as [19,83,84,94,95]

$$E_k = \tfrac{1}{2}\mathcal{M}(\theta)\dot{R}^2, \quad \text{(E1)}$$

where $\mathcal{M}(\theta)$ is the reduced mass of the pinned torus bubble for contact angle oscillations [Fig. 7(a)] and $\dot{R}$ is the velocity of the bubble interface, which can be approximated by

$$\dot{R} = \frac{1}{S_b}\frac{dV_b}{d\theta}\dot{\theta}.$$

For radial oscillations of a spherical bubble of radius R, $\mathcal{M}$ can be determined analytically to be $\mathcal{M} = 4\pi\rho_w R^3$. However, for a torus bubble, we need to calculate $\mathcal{M}$ numerically, by implementing potential flow theory [96] on a finite element method (FEM) grid in MATLAB [97].

First, at a given θ, $dV_b/d\theta$ is calculated from the slope of V_b versus θ in Fig. S5(f) [49]. The continuity equation is invoked in the liquid surrounding the bubble in an axisymmetric coordinate system,

$$\nabla^2\phi = 0, \quad \text{(E2)}$$

where ϕ is the velocity potential. For a contact angle velocity $\dot{\theta}$, we calculate the radial $(\Delta R/\Delta t)$ and axial $(\Delta Z/\Delta t)$ velocities of the tracer points on the bubble surface (Fig. S10b in the Supplemental Material [49]). These velocities are interpolated on the mesh points of the bubble surface, which act as boundary conditions. A far-field boundary condition $\phi = \phi_0$ is applied on the liquid boundary far from the bubble. On the remaining boundary surfaces, zero-flux boundary conditions are applied, $d\phi/dn = 0$, where n is the normal direction to the surface. The solution for the velocity potential is used to obtain the radial liquid velocity $u_r = \partial\phi/\partial r$ and axial liquid velocity $u_z = \partial\phi/\partial z$, which are integrated over the mesh triangles to obtain the total liquid kinetic energy [94,95]

$$E_k = \int_V \rho_w\frac{1}{2}\left(u_r^2 + u_z^2\right)dV. \quad \text{(E3)}$$

Here, the density of the liquid is taken as $\rho_w = 1000\ \text{kg/m}^3$. From Eqs. (E1) and (E3), $\mathcal{M}(\theta)$ is obtained.

[1] T. L. Hill, A different approach to nanothermodynamics, Nano Lett. **1**, 273 (2001).

[2] N. Kavokine, R. R. Netz, and L. Bocquet, Fluids at the nanoscale: From continuum to subcontinuum transport, Annu. Rev. Fluid Mech. **53**, 377 (2021).

[3] N. S. Dhillon, J. Buongiorno, and K. K. Varanasi, Critical heat flux maxima during boiling crisis on textured surfaces, Nat. Commun. **6**, 8247 (2015).

[4] A. Asai, Application of the nucleation theory to the design of bubble jet printers, Jpn. J. Appl. Phys. **28**, 909 (1989).

[5] M. Jiang, Y. Wang, F. Liu, H. Du, Y. Li, H. Zhang, S. To, S. Wang, C. Pan, J. Yu *et al.*, Inhibiting the Leidenfrost effect above 1, 000°C for sustained thermal cooling, Nature **601**, 568 (2022).

[6] S. Nukiyama, Memories of my research on boiling, Int. J. Heat Mass Transfer **27**, 955 (1984).

[7] J. H. Lienhard and L. C. Witte, An historical review of the hydrodynamic theory of boiling, Rev. Chem. Eng. **3**, 187 (1985).

[8] L. Chen, Y. S. Tian, and T. G. Karayiannis, The effect of tube diameter on vertical two-phase flow regimes in small tubes, Int. J. Heat Mass Transfer **49**, 4220 (2006).

[9] S. G. Kandlikar and A. V. Bapat, Evaluation of jet impingement, spray and microchannel chip cooling options for high heat flux removal, Heat Transfer Eng. **28**, 911 (2007).

[10] T. P. Allred, J. A. Weibel, and S. V. Garimella, Enabling Highly Effective Boiling from Superhydrophobic Surfaces, Phys. Rev. Lett. **120**, 174501 (2018).

[11] H. J. Cho, J. P. Mizerak, and E. N. Wang, Turning bubbles on and off during boiling using charged surfactants, Nat. Commun. **6**, 8599 (2015).

[12] D. I. Yu, H. J. Kwak, H. Noh, H. S. Park, K. Fezzaa, and M. H. Kim, Synchrotron x-ray imaging visualization study of capillary-induced flow and critical heat flux on surfaces with engineered micropillars, Sci. Adv. **4**, e1701571 (2018).

[13] N. Saneie, V. Kulkarni, B. Treska, K. Fezzaa, N. Patankar, and S. Anand, Microbubble dynamics and heat transfer in boiling droplets, Int. J. Heat Mass Transfer **176**, 121413 (2021).

[14] N. Saneie, V. Kulkarni, K. Fezzaa, N. A. Patankar, and S. Anand, Boiling transitions during droplet contact on superheated nano/micro-structured surfaces, ACS Appl. Mater. Interfaces **14**, 15774 (2022).

[15] S.-H. Lee, S. J. Lee, J. S. Lee, K. Fezzaa, and J. H. Je, Transient dynamics in drop impact on a superheated surface, Phys. Rev. Fluids **3**, 124308 (2018).

[16] E. Popov, L. He, E. Dominguez-Ontiveros, and Y. Melnichenko, Detection of vapor nanobubbles by small angle neutron scattering (SANS), Appl. Phys. Lett. **112**, 153704 (2018).

[17] K. H. Chu, R. Enright, and E. N. Wang, Structured surfaces for enhanced pool boiling heat transfer, Appl. Phys. Lett. **100**, 241603 (2012).

[18] V. K. Dhir, Boiling heat transfer, Annu. Rev. Fluid Mech. **30**, 365 (1998).

[19] A. Prosperetti, Vapor bubbles, Annu. Rev. Fluid Mech. **49**, 221 (2017).

[20] D. Qiu, V. Dhir, D. Chao, M. Hasan, E. Neumann, G. Yee, and A. Birchenough, Single-bubble dynamics during pool boiling under low gravity conditions, J. Thermophys. Heat Transfer **16**, 336 (2002).

[21] Y. Nam, E. Aktinol, V. K. Dhir, and Y. S. Ju, Single bubble dynamics on a superhydrophilic surface with artificial nucleation sites, Int. J. Heat Mass Transfer **54**, 1572 (2011).

[22] J. Y. Lee, M.-H. Kim, M. Kaviany, and S. Y. Son, Bubble nucleation in microchannel flow boiling using single artificial cavity, Int. J. Heat Mass Transfer **54**, 5139 (2011).

[23] S. Witharana, B. Phillips, S. Strobel, H. D. Kim, T. McKrell, J. B. Chang, J. Buongiorno, K. K. Berggren, L. Chen, and Y. Ding, Bubble nucleation on nano- to micro-size cavities and posts: An experimental validation of classical theory, J. Appl. Phys. **112**, 064904 (2012).

[24] E. V. Levine, M. M. Burns, and J. A. Golovchenko, Nanoscale dynamics of Joule heating and bubble nucleation in a solid-state nanopore, Phys. Rev. E **93**, 013124 (2016).

[25] Y. Wang, M. E. Zaytsev, H. L. The, J. C. Eijkel, H. J. Zandvliet, X. Zhang, and D. Lohse, Vapor and gas-bubble growth dynamics around laser-irradiated, water-immersed plasmonic nanoparticles, ACS Nano **11**, 2045 (2017).

[26] L. Hou, M. Yorulmaz, N. R. Verhart, and M. Orrit, Explosive formation and dynamics of vapor nanobubbles around a continuously heated gold nanosphere, New J. Phys. **17**, 013050 (2015).

[27] S. Nag, Y. Tomo, K. Takahashi, and M. Kohno, Mechanistic insights into nanobubble merging studied using in situ liquid-phase electron microscopy, Langmuir **37**, 874 (2021).

[28] X. Deng, Y. Shan, X. Meng, Z. Yu, X. Lu, Y. Ma, J. Zhao, D. Qiu, X. Zhang, Y. Liu *et al.*, Direct measuring of single–heterogeneous bubble nucleation mediated by surface topology, Proc. Natl. Acad. Sci. USA **119**, e2205827119 (2022).

[29] L. Luo and H. S. White, Electrogeneration of single nanobubbles at sub-50-nm-radius platinum nanodisk electrodes, Langmuir **29**, 11169 (2013).

[30] Q. Chen, L. Luo, H. Faraji, S. W. Feldberg, and H. S. White, Electrochemical measurements of single H_2 nanobubble nucleation and stability at Pt nanoelectrodes, J. Phys. Chem. Lett. **5**, 3539 (2014).

[31] Y. X. Hu, Y. L. Ying, R. Gao, R. J. Yu, and Y. T. Long, Characterization of the dynamic growth of the nanobubble within the confined glass nanopore, Anal. Chem. **90**, 12352 (2018).

[32] X. Fu, B. Chen, J. Tang, and A. H. Zewail, Photoinduced nanobubble-driven superfast diffusion of nanoparticles imaged by 4D electron microscopy, Sci. Adv. **3**, e1701160 (2017).

[33] G. Lajoinie, M. Visscher, E. Blazejewski, G. Veldhuis, and M. Versluis, Three-phase vaporization theory for laser-activated microcapsules, Photoacoustics **19**, 100185 (2020).

[34] M. Versluis, B. Schmitz, A. Von der Heydt, and D. Lohse, How snapping shrimp snap: Through cavitating bubbles, Science **289**, 2114 (2000).

[35] S. Paul, W.-L. Hsu, M. Magnini, L. R. Mason, Y. Ito, Y.-L. Ho, O. K. Matar, and H. Daiguji, Analysis and control of vapor bubble growth inside solid-state nanopores, J. Therm. Sci. Technol. **16**, JTST0007 (2021).

[36] F. Li, S. R. Gonzalez-Avila, D. M. Nguyen, and C.-D. Ohl, Oscillate boiling from microheaters, Phys. Rev. Fluids **2**, 014007 (2017).

[37] D. M. Nguyen, L. Hu, J. Miao, and C.-D. Ohl, Oscillate Boiling from Electrical Microheaters, Phys. Rev. Appl. **10**, 044064 (2018).

[38] G. Nagashima, E. V. Levine, D. P. Hoogerheide, M. M. Burns, and J. A. Golovchenko, Superheating and Homogeneous Single Bubble Nucleation in a Solid-State Nanopore, Phys. Rev. Lett. **113**, 024506 (2014).

[39] S. Paul, W.-L. Hsu, M. Magnini, L. R. Mason, Y.-L. Ho, O. K. Matar, and H. Daiguji, Single-bubble dynamics in nanopores: Transition between homogeneous and heterogeneous nucleation, Phys. Rev. Res. **2**, 043400 (2020).

[40] Z. Zhao, S. Glod, and D. Poulikakos, Pressure and power generation during explosive vaporization on a thin-film microheater, Int. J. Heat Mass Transfer **43**, 281 (2000).

[41] O. Supponen, D. Obreschkow, P. Kobel, N. Dorsaz, and M. Farhat, Detailed experiments on weakly deformed cavitation bubbles, Exp. Fluids **60**, 33 (2019).

[42] S. Glod, D. Poulikakos, Z. Zhao, and G. Yadigaroglu, An investigation of microscale explosive vaporization of water on an ultrathin Pt wire, Int. J. Heat Mass Transfer **45**, 367 (2002).

[43] D. M. Nguyen, O. Supponen, J. Miao, M. Farhat, and C.-D. Ohl, Gravity-independent oscillate boiling, Microgravity Sci. Technol. **31**, 767 (2019).

[44] R. Medvedev, A. Chernov, and D. Karpov, Calculations of pulsation period of a toroidal bubble during diaphragm discharge in electrolyte, Int. J. Heat Mass Transfer **64**, 743 (2013).

[45] D. Lohse and X. Zhang, Pinning and gas oversaturation imply stable single surface nanobubbles, Phys. Rev. E **91**, 031003(R) (2015).

[46] S. Nag, Y. Tomo, H. Teshima, K. Takahashi, and M. Kohno, Dynamic interplay between interfacial nanobubbles: Oversaturation promotes anisotropic depinning and bubble coalescence, Phys. Chem. Chem. Phys. **23**, 24652 (2021).

[47] C. E. Brennen, *Cavitation and Bubble Dynamics* (Cambridge University Press, New York, 2014).

[48] W. Lauterborn and T. Kurz, Physics of bubble oscillations, Rep. Prog. Phys. **73**, 106501 (2010).

[49] See Supplemental Material at http://link.aps.org/supplemental/10.1103/PhysRevResearch.4.043110 for include information about nanopore SEM images (S1), hydrophone positioning (S2), onset of nucleate boiling results for 1134 nm pore (S3), torus bubble dynamics (S4). Sections 5–8 contain additional boiling transition results for the expanded 250 nm pore (S5),

340 nm pore (S6), 460 nm pore (S7), and 420 nm pore (S8) respectively.

[50] E. G. Radulescu, P. A. Lewin, A. Goldstein, and A. Nowicki, Hydrophone spatial averaging corrections from 1 to 40 MHz, IEEE Trans. Ultrason. Ferroelectr. Freq. Control **48**, 1575 (2001).

[51] A. Hurrell, Voltage to pressure conversion: Are you getting "phased" by the problem? J. Phys.: Conf. Ser. **1**, 57 (2004).

[52] Q. Wang, J. Gu, Z. Li, and W. Yao, Dynamic modeling of bubble growth in vapor–liquid phase change covering a wide range of superheats and pressures, Chem. Eng. Sci. **172**, 169 (2017).

[53] C. T. Chin, C. Lancée, J. Borsboom, F. Mastik, M. E. Frijlink, N. de Jong, M. Versluis, and D. Lohse, Brandaris 128: A digital 25 million frames per second camera with 128 highly sensitive frames, Rev. Sci. Instrum. **74**, 5026 (2003).

[54] K. Namura, S. Okai, S. Kumar, K. Nakajima, and M. Suzuki, Self-oscillation of locally heated water vapor microbubbles in degassed water, Adv. Mater. Interfaces **7**, 2000483 (2020).

[55] T. Jollans and M. Orrit, Explosive, oscillatory, and Leidenfrost boiling at the nanoscale, Phys. Rev. E **99**, 063110 (2019).

[56] Y. Hou, M. Yu, X. Chen, Z. Wang, and S. Yao, Recurrent filmwise and dropwise condensation on a beetle mimetic surface, ACS Nano **9**, 71 (2015).

[57] J. Eshraghi, A. M. Ardekani, and P. P. Vlachos, Data assimilation for modeling cavitation bubble dynamics, Exp. Fluids **62**, 90 (2021).

[58] M. Alheshibri, J. Qian, M. Jehannin, and V. S. Craig, A history of nanobubbles, Langmuir **32**, 11086 (2016).

[59] D. Dockar, L. Gibelli, and M. K. Borg, Forced oscillation dynamics of surface nanobubbles, J. Chem. Phys. **153**, 184705 (2020).

[60] V. Viasnoff, U. Bockelmann, A. Meller, H. Isambert, L. Laufer, and Y. Tsori, Localized Joule heating produced by ion current focusing through micron-size holes, Appl. Phys. Lett. **96**, 163701 (2010).

[61] M. Tsutsui, A. Arima, K. Yokota, Y. Baba, and T. Kawai, Ionic heat dissipation in solid-state pores, Sci. Adv. **8**, eabl7002 (2022).

[62] S. Paul, Y. Hanada, B. Lan, H. Daiguji, K.-C. Liang, and W.-L. Hsu, Data analysis platform for nanobubble characterization of solid-state nanopores, in *Proceedings of the 2022 IEEE 17th International Conference on Nano/Micro Engineered and Molecular Systems (NEMS)* (IEEE, New York, 2022), pp. 205–210.

[63] J. Zou, H. Zhang, Z. Guo, Y. Liu, J. Wei, Y. Huang, and X. Zhang, Surface nanobubbles nucleate liquid boiling, Langmuir **34**, 14096 (2018).

[64] W. Lauterborn, Numerical investigation of nonlinear oscillations of gas bubbles in liquids, J. Acoust. Soc. Am. **59**, 283 (1976).

[65] W. Lauterborn and E. Suchla, Bifurcation Superstructure in a Model of Acoustic Turbulence, Phys. Rev. Lett. **53**, 2304 (1984).

[66] W. Lauterborn and E. Cramer, Subharmonic Route to Chaos Observed in Acoustics, Phys. Rev. Lett. **47**, 1445 (1981).

[67] A. Gadaleta, C. Sempere, S. Gravelle, A. Siria, R. Fulcrand, C. Ybert, and L. Bocquet, Sub-additive ionic transport across arrays of solid-state nanopores, Phys. Fluids **26**, 012005 (2014).

[68] M. Shoji, Studies of boiling chaos: A review, Int. J. Heat Mass Transfer **47**, 1105 (2004).

[69] V. K. Dhir, G. R. Warrier, and E. Aktinol, Numerical simulation of pool boiling: A review, J. Heat Transfer **135**, 061502 (2013).

[70] Y. Hao and A. Prosperetti, The dynamics of vapor bubbles in acoustic pressure fields, Phys. Fluids **11**, 2008 (1999).

[71] S. Maheshwari, M. van der Hoef, A. Prosperetti, and D. Lohse, Dynamics of formation of a vapor nanobubble around a heated nanoparticle, J. Phys. Chem. C **122**, 20571 (2018).

[72] J. Lee, T. Laoui, and R. Karnik, Nanofluidic transport governed by the liquid/vapour interface, Nat. Nanotechnol. **9**, 317 (2014).

[73] V. P. Carey, *Liquid–Vapor Phase-Change Phenomena: An Introduction to the Thermophysics of Vaporization and Condensation Processes in Heat Transfer Equipment* (CRC Press, Boca Raton, FL, 2020).

[74] Z. Wang, W.-L. Hsu, S. Tsuchiya, S. Paul, A. Alizadeh, and H. Daiguji, Joule heating effects on transport-induced-charge phenomena in an ultrathin nanopore, Micromachines **11**, 1041 (2020).

[75] D. Lohse and X. Zhang, Surface nanobubbles and nanodroplets, Rev. Mod. Phys. **87**, 981 (2015).

[76] Y. Liu, S. Bernardi, and A. Widmer-Cooper, Stability of pinned surface nanobubbles against expansion: Insights from theory and simulation, J. Chem. Phys. **153**, 024704 (2020).

[77] M. P. Brenner and D. Lohse, Dynamic Equilibrium Mechanism for Surface Nanobubble Stabilization, Phys. Rev. Lett. **101**, 214505 (2008).

[78] N. D. Petsev, M. S. Shell, and L. G. Leal, Dynamic equilibrium explanation for nanobubbles' unusual temperature and saturation dependence, Phys. Rev. E **88**, 010402(R) (2013).

[79] N. Kameda and S. Nakabayashi, Size-induced sign inversion of line tension in nanobubbles at a solid/liquid interface, Chem. Phys. Lett. **461**, 122 (2008).

[80] B. H. Tan, H. An, and C.-D. Ohl, Resolving the Pinning Force of Nanobubbles with Optical Microscopy, Phys. Rev. Lett. **118**, 054501 (2017).

[81] J. R. Seddon and D. Lohse, Nanobubbles and micropancakes: gaseous domains on immersed substrates, J. Phys.: Condens. Matter **23**, 133001 (2011).

[82] A. Prosperetti, The speed of sound in a gas–vapour bubbly liquid, Interface Focus **5**, 20150024 (2015).

[83] O. Vincent and P. Marmottant, On the statics and dynamics of fully confined bubbles, J. Fluid Mech. **827**, 194 (2017).

[84] T. G. Leighton and A. J. Walton, An experimental study of the sound emitted from gas bubbles in a liquid, Eur. J. Phys. **8**, 98 (1987).

[85] A. Gray, E. Abbena, and S. Salamon, *Modern Differential Geometry of Curves and Surfaces with Mathematica* (Chapman and Hall/CRC, Boca Raton, FL, 2017).

[86] W. Wagner and A. Pruß, The IAPWS Formulation 1995 for the thermodynamic properties of ordinary water substance for general and scientific use, J. Phys. Chem. Ref. Data **31**, 387 (2002).

[87] D. J. E. Harvie, An implicit finite volume method for arbitrary transport equations, ANZIAM J. **52**, 1126 (2012).

[88] V. Dimitrov, U. Mirsaidov, D. Wang, T. Sorsch, W. Mansfield, J. Miner, F. Klemens, R. Cirelli, S. Yemenicioglu, and G. Timp, Nanopores in solid-state membranes engineered for single molecule detection, Nanotechnology **21**, 065502 (2010).

[89] C. T. Avedisian, The homogeneous nucleation limits of liquids, J. Phys. Chem. Ref. Data **14**, 695 (1985).

[90] J. R. T. Seddon, H. J. W. Zandvliet, and D. Lohse, Knudsen Gas Provides Nanobubble Stability, Phys. Rev. Lett. **107**, 116101 (2011).

[91] V. S. J. Craig, Very small bubbles at surfaces-the nanobubble puzzle, Soft Matter **7**, 40 (2011).

[92] E. Aursand and T. Ytrehus, Comparison of kinetic theory evaporation models for liquid thin-films, Int. J. Multiphase Flow **116**, 67 (2019).

[93] V. N. Alekseev, Nonsteady behavior of a vapor bubble in an ultrasonic-field, Sov. Phys. Acoust. **22**, 104 (1976).

[94] A. Prosperetti, Free oscillations of drops and bubbles: The initial-value problem, J. Fluid Mech. **100**, 333 (1980).

[95] Z. Zhang, Y. Wang, Y. Amarouchene, R. Boisgard, H. Kellay, A. Würger, and A. Maali, Near-Field Probe of Thermal Fluctuations of a Hemispherical Bubble Surface, Phys. Rev. Lett. **126**, 174503 (2021).

[96] P. K. Kundu, I. M. Cohen, and D. R. Dowling, *Fluid Mechanics* (Academic Press, Waltham, MA, 2015).

[97] MATLAB, *9.6.0.1174912 (R2019a) Update 5* (The MathWorks Inc., Natick, MA, 2019).